



Politecnico
di Torino



Université
Paris Cité

Politecnico di Torino - Université Paris Cité

International double degree program NanoQuad:
Nanotechnologies for ICTs and Quantum Devices
Academic year 2022/2023
June 2023

On-chip engineering of frequency quantum states of light for quantum information

Italo Pio DE SIMEONE

Supervisor:

Prof. Sara DUCCI

Relators:

Prof. Carlo RICCIARDI

Prof. Maria Luisa DELLA ROCCA

Contents

Introduction	1
Presentation of the lab	1
Internship project	2
1 Nonlinear optical processes in AlGaAs	3
1.1 Introduction to nonlinear optical processes	3
1.1.1 Propagation in a nonlinear medium	4
1.1.2 Phase matching	4
1.2 GaAs and AlGaAs optical properties	5
2 Design of the counterpropagating source	7
2.1 Dimensioning of the waveguide	7
2.2 Study of the effect of mirror deposition on the facets reflectivity	9
2.3 Joint Spectral Amplitude	10
2.4 Fabry-Pérot cavity effect	12
2.5 Hong-Ou-Mandel interference in the single interaction case	13
2.6 Hong-Ou-Mandel interference in the double interaction case	15
2.7 Dry etched waveguide	16
3 Fabrication and characterization of samples with high reflectivity mirrors	19
3.1 Deposition technique	19
3.2 Measurement of Fabry Pérot spectra before mirror deposition	20
3.3 Measurement of Fabry Pérot spectra after mirror deposition	22
4 Photon pairs generation	23
5 Conclusions and perspectives	24

Acronyms

BS Beam Splitter.
CAR Coincidence to Accidental Ratio.
DBR Distributed Bragg Reflectors.
DFG Difference Frequency Generation.
FDE Finite Difference Eigenmode.
FDTD Finite Difference Time Domain.
FSS Fine Structure Splitting.
HOM Hong-Ou-Mandel.
HPF Hybrid Polarization Frequency.
IBAD Ion Beam Assisted Deposition.
JSA Joint Spectral Amplitude.
JSI Joint Spectral Intensity.
OSA Optical Spectrum Analyzer.
PPLN Periodically Poled Lithium Niobate.
QD Quantum Dots.
QPM Quasi-Phase Matching.
SEM Scanning Electron Microscope.
SFG Sum Frequency Generation.
SFWM Spontaneous Four Wave Mixing.
SHG Second Harmonic Generation.
SLM Spatial Light Modulator.
SNSPD Superconductive Nanowire Single Photon Detector.
SPDC Spontaneous Parametric Down Conversion.
TT Time Tagger.

Introduction

Context: **Quantum technology** is an emerging field of physics and engineering, encompassing technologies that rely on the properties of quantum mechanics, especially quantum entanglement, quantum superposition, and quantum tunneling. This field is divided into four main research topics:

- *Quantum computing*, where quantum properties of systems like trapped ions and superconducting circuits are used to implement algorithms that could be in principle much more efficient than classical ones, exponentially reducing the time required for calculations;
- *Quantum simulation* is closely related to quantum computing; using a different approach, it consists in using a controllable and easily accessible quantum system to analogically simulate a less accessible and controllable one;
- *Quantum metrology* exploits the inherent high sensibility and sensitivity of quantum systems to produce very accurate and precise measurements;
- *Quantum communication* utilizes quantum properties of photons (like entanglement) to transmit information in an unconditionally secure way.

These 4 pillars are based on a common foundation, generally referred to as “enabling technologies”, which brings together all the research on materials, devices, theoretical tools in physics and information theory required for application developments.

Photons have proven to be the most reliable platform for quantum communications for several reasons: they travel at the speed of light, they can exploit pre-existing classical networks (like optical fibers and satellites), they exhibit quantum behavior at room temperature and they are resistant against noise and decoherence. The ability to generate and engineer quantum states of light is therefore crucial for the development of this technology. In this work we focus on sources of photon pairs, that can be divided into two main categories: deterministic and probabilistic.

Deterministic sources ideally generate a pair each time a trigger signal is sent; they can be implemented using radiative cascades in atoms, as it was done by A. Aspect, P. Grangier and G. Roger [1] [2] in their experimental implementation of the “Gedankenexperiment” with calcium atoms to test the violation of Bell’s inequality [3].

Probabilistic sources exploit down-conversion of a pump laser in nonlinear crystals. Several materials are available, such as LiNbO₃ [4] and GaAs for Spontaneous Parametric Down Conversion (SPDC) (exploiting a second order nonlinearity) and Si for Spontaneous Four Wave Mixing (SFWM) (exploiting a third order nonlinearity). Since they are based on a probabilistic process, they are not able to produce photons on demand; however, they allow for simpler setups (room temperature operation, no need for vacuum chambers), can take advantage of well established fabrication technologies and enable high quality quantum state generation exploiting a large variety of degrees of freedom.

Today, thanks to the progress in miniaturization and scaling, deterministic sources are mainly implemented using biexciton-exciton cascade in semiconductor Quantum Dots (QD), as it was first proposed by Benson et al. [5]. They can be integrated with other structures to increase the collection efficiency, such as microcavities [6] or Distributed Bragg Reflectors (DBR) [7]. One of the main challenges in their development is overcoming the Fine Structure Splitting (FSS), which reduces the degree of entanglement and indistinguishability [8]. Probabilistic sources, on the other hand, moved from bulk crystals to integrated sources, such as Silicon microring resonators [9] for SFWM and AlGaAs waveguides [10] for SPDC, which can be integrated in monolithic chips that contain all the components needed for the implementation of quantum information protocols [11].

Presentation of the lab

I carried out my internship in the Quantum Information and Technologies (QITe) team of the Laboratory Matériaux et Phénomènes Quantiques (MPQ), a mixed research unit of Université Paris Cité and CNRS. The laboratory specializes in the study of frontier quantum materials and in the development of novel quantum devices. These activities rely on a large spectrum of theoretical and experimental expertise in material physics, transport and optics, and technological platforms of cleanroom fabrication, spectroscopy and high-resolution electronic microscopy.

The QITe team develops platforms and integrated photonic devices for quantum information; it is organized in three research axes: quantum photonics, trapped ions and theory. During my internship I was part of the quantum photonics group, which works on the design, fabrication and characterization of

III-V semiconductor sources of entangled photons working at room temperature at telecom wavelength. The group develops several projects:

- Counterpropagating entangled photon sources, on which I worked during my internship, particularly suited for quantum simulations and quantum metrology;
- Copropagating entangled photon sources, particularly suited for communication protocols exploiting broadband entangled photon states;
- Waveguide array networks for the implementation of spatial modes entanglement;
- Hybrid III-V/SOI entangled photon sources, to combine the assets of the two platforms.

Internship project

My internship focuses on a waveguide microcavity emitting quantum states of light in a transverse pump configuration, and in particular on the engineering of the spectrum of the emitted two-photon state in view of the realization of an ion-photon interface, a key element for the inclusion of trapped ions nodes in quantum networks. To pursue this objective and achieve ion-photon entanglement, a wavelength and spectral width match between the ion and photon systems is required. During my internship, I worked on the spectral narrowing of the emitted photon pairs; this enabled me to integrate the team's work by familiarizing myself with numerical simulations, cleanroom fabrication and sample characterization in both classical and quantum optical regime.

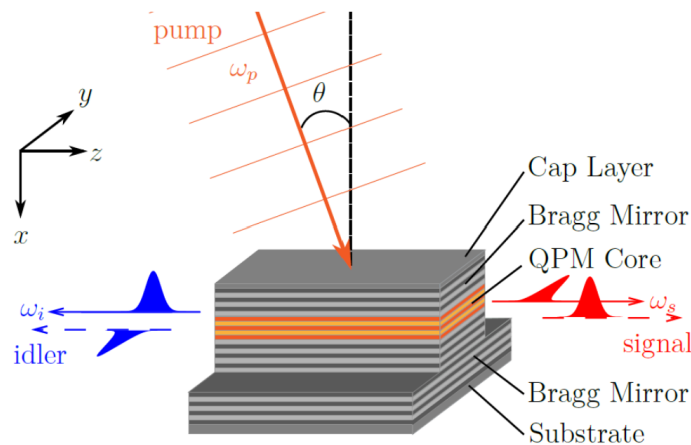


Figure 1: Sketch of the source based on the counterpropagating phasematching scheme under transverse pumping

The report is structured as it follows: chapter 1 consists an overview of second order nonlinear processes in crystals, with particular focus on AlGaAs. In chapter 2 I present the results of my numerical simulations concerning the waveguide's facet reflectivity and the emitted biphoton state. The experimental characterization of my sample is detailed in chapter 3, while in chapter 4 I describe the experimental setup used for the photon pairs generation. In the end, in chapter 5, I summarize the results of my work and present the future development of this project.

1 Nonlinear optical processes in AlGaAs

1.1 Introduction to nonlinear optical processes

This analysis follows the book Nonlinear Optics by R. Boyd [12]. When a weak electric field $E(t)$ impinges on a material, this will display a linear response that we express through the polarization density $P(t)$:

$$P(t) = \epsilon_0 \chi^{(1)} E(t) \quad (1.1)$$

where ϵ_0 is the vacuum permittivity and $\chi^{(1)}$ is called the *linear susceptibility* of the material. More in general, the polarization can be expressed as a power series of the field:

$$\begin{aligned} P(t) &= \epsilon_0 \left[\chi^{(1)} E(t) + \chi^{(2)} E^2(t) + \chi^{(3)} E^3(t) + \dots \right] \\ &= P^{(1)}(t) + P^{(2)}(t) + P^{(3)}(t) + \dots \end{aligned} \quad (1.2)$$

with $\chi^{(2)}$ and $\chi^{(3)}$, respectively, the *second order* and *third order nonlinear susceptibilities*. For simplicity, the fields were taken as scalar quantities and therefore the susceptibilities are in turn scalar. In the general case where one considers vector fields, the $\chi^{(m)}$ susceptibility becomes a $m + 1$ rank tensor. Its value decreases very fast with increasing order: to give an order of magnitude, we can say that:

$$\begin{aligned} \chi^{(1)} &\sim 1 \text{ m/V} \\ \chi^{(2)} &\sim 10^{-12} \text{ m/V} \\ \chi^{(3)} &\sim 10^{-24} \text{ m/V} \end{aligned}$$

Hence, in order to observe nonlinear effects, intense fields are required, like the ones produced by laser sources. Moreover, $\chi^{(2)}$ is identically zero for centrosymmetric media (i.e. crystals with inversion symmetry), like Silicon. As a consequence, in order to exploit second order nonlinear processes, one has to resort to non-centrosymmetric crystals, like LiNbO₃ and AlGaAs. In this kind of media, several kinds of second order nonlinear processes (also referred as “Three wave mixing” because they involve three waves at frequency $\omega_1, \omega_2, \omega_3$) can happen:

- **Sum Frequency Generation (SFG)** (Figure 2a): two pump fields of frequency ω_1 and ω_2 generate a third field at frequency $\omega_3 = \omega_1 + \omega_2$
- **Second Harmonic Generation (SHG)**: a particular case of SFG with $\omega_1 = \omega_2 = \omega$, hence the generated field has frequency 2ω
- **Difference Frequency Generation (DFG)**: two pump fields of frequency ω_1 and ω_2 generate a third field at frequency $\omega_3 = \omega_1 - \omega_2$
- **Spontaneous Parametric Down Conversion (SPDC)** (Figure 2b): it is the inverse process of SFG, i.e. one pump field ω_p generates two fields ω_s, ω_i (often called *signal* and *idler*) such that $\omega_s + \omega_i = \omega_p$ (energy conservation). This process cannot be entirely described classically; however, a semiclassical description is possible by considering a DFG interaction of the pump field with vacuum fluctuations.



Figure 2: Sketch illustrating two three wave mixing processes : a) Sum Frequency Generation; b) Spontaneous Parametric Down Conversion

1.1.1 Propagation in a nonlinear medium

Let us start from Maxwell equation for a material with no free charges ($\rho = 0$) and no free currents ($\mathbf{J} = 0$):

$$\nabla \times \mathbf{E} = -\frac{\partial \mathbf{B}}{\partial t} \quad (1.3)$$

$$\nabla \times \mathbf{H} = -\frac{\partial \mathbf{D}}{\partial t} \quad (1.4)$$

$$\nabla \cdot \mathbf{B} = 0 \quad (1.5)$$

$$\nabla \cdot \mathbf{D} = 0 \quad (1.6)$$

They can be combined to obtain:

$$\nabla^2 \mathbf{E} - \frac{1}{c^2} \frac{\partial^2 \mathbf{E}}{\partial t^2} = \frac{1}{\epsilon_0 c^2} \frac{\partial^2 \mathbf{P}}{\partial t^2} \quad (1.7)$$

The polarization vector can be split in its linear and nonlinear part:

$$\mathbf{P} = \mathbf{P}^L + \mathbf{P}^{NL} \quad (1.8)$$

Similarly for the displacement vector:

$$\mathbf{D} = \mathbf{D}^{(1)} + \mathbf{P}^{NL} \quad (1.9)$$

where the linear part is:

$$\mathbf{D}^{(1)} = \epsilon_0 \mathbf{E} + \mathbf{P}^{(1)} \quad (1.10)$$

In a lossless, dispersionless and isotropic media:

$$\mathbf{D}^{(1)} = \epsilon_0 \epsilon^{(1)} \mathbf{E} \quad (1.11)$$

with $\epsilon^{(1)}$ the real, frequency independent dielectric constant. Hence, Equation 1.7 reduces to:

$$\nabla^2 \mathbf{E} - \frac{n^2}{c^2} \frac{\partial^2 \mathbf{E}}{\partial t^2} = \frac{1}{\epsilon_0 c^2} \frac{\partial^2 \mathbf{P}^{NL}}{\partial t^2} \quad (1.12)$$

1.1.2 Phase matching

Consider a SFG process that generates a field \mathbf{E}_3 from two fields \mathbf{E}_1 and \mathbf{E}_2 propagating along the z direction (analogous considerations can be applied to DFG and SPDC). For simplicity, let us also consider scalar fields, dropping the vectorial notation:

$$\begin{aligned} E_1 &= A_1 e^{i(k_1 z - \omega_1 t)} + c.c. \\ E_2 &= A_2 e^{i(k_2 z - \omega_2 t)} + c.c. \\ E_3 &= A_3 e^{i(k_3 z - \omega_3 t)} + c.c. \end{aligned} \quad (1.13)$$

where

$$k_i = \frac{n_i \omega_i}{c}, \quad n_i = n(\omega_i), \quad i = 1, 2, 3 \quad (1.14)$$

The output intensity can be proven to be [12]:

$$I_3 = \frac{8d_{eff}^2 \omega_3^2 I_1 I_2}{n_1 n_2 n_3 \epsilon_0 c^2} L^2 \text{sinc}^2 \left(\frac{\Delta k L}{2} \right) \quad (1.15)$$

with I_1, I_2 the two input intensities, L the medium length, $d_{eff} = \frac{1}{2} \chi^{(2)}$ and

$$\Delta k = k_1 + k_2 - k_3 \quad (1.16)$$

the *phase mismatch*. As it can be seen from Figure 3a, the effect of phase mismatch on the output intensity (and therefore on the conversion efficiency) is very important: it is therefore crucial to satisfy the relation

$$\Delta k = 0 \quad (1.17)$$

called *phase matching condition*. However, this condition, that can be rewritten as:

$$\frac{n_1 \omega_1}{c} + \frac{n_2 \omega_2}{c} = \frac{n_3 \omega_3}{c} \quad (1.18)$$

is not straightforward to be satisfied because of the dispersion of the refractive index. In bulk crystals, different solutions can be implemented:

- a) Exploit the *birefringence* of the crystal, i.e. the dependance of the refractive index on the field polarization. This can be done in highly birefringent nonlinear crystals like KDP and LiNbO₃ [13].
- b) *Quasi-Phase Matching* (QPM): as it can be seen in Figure 3b, in case of phase mismatch the field intensity oscillates while it propagates inside the structure. The idea of QPM is to invert the sign of d_{eff} when this oscillation is at its maximum: in this way the nonlinear interaction continues to be constructive instead of becoming destructive. By doing this periodically in correspondence of every extrema of the oscillation, a net increase of the intensity can be achieved. This can be realized by periodically poling a nonlinear crystal, i.e. periodically changing the orientation of its crystallographic axis, as it is done for instance in PPLN [14].

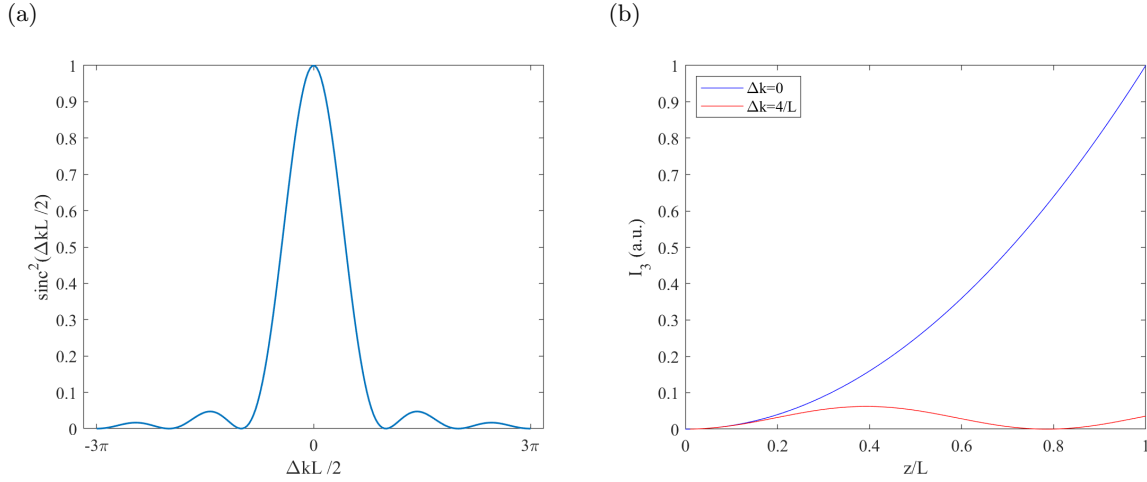


Figure 3: (a) Effect of phase mismatch on SFG efficiency (b) Optical intensity for a perfect phase match (blue) and a phase mismatch $\Delta k = 4/L$ (red)

1.2 GaAs and AlGaAs optical properties

GaAs is a widely used material in photonics and optoelectronics thanks to its several assets:

- Room temperature operation at telecom wavelength;
- High second order non linearity [15];
- High electro-optic effect [16];
- Direct band gap, allowing the monolithic integration of electrically driven laser and nonlinear optical medium [17];

GaAs has a zincblende crystal structure with $\bar{4}3m$ symmetry; if we introduce the tensor:

$$d_{ijk} = \frac{1}{2}\chi_{ijk}^{(2)} \quad (1.19)$$

we can exploit GaAs permutation symmetries to define an equivalent contracted matrix d_{il} according to [12]:

$$\begin{array}{c|cccccc} jk & 11 & 22 & 33 & 23/32 & 31/13 & 12/21 \\ \hline l & 1 & 2 & 3 & 4 & 5 & 6 \end{array}$$

Hence, $\chi_{ijk}^{(2)}$ is reduced to a 3x6 matrix:

$$d_{il} = \begin{pmatrix} d_{11} & d_{12} & d_{13} & d_{14} & d_{15} & d_{16} \\ d_{16} & d_{22} & d_{23} & d_{24} & d_{14} & d_{12} \\ d_{15} & d_{24} & d_{33} & d_{23} & d_{13} & d_{14} \end{pmatrix} \quad (1.20)$$

Moreover, the $\bar{4}3m$ symmetry imposes only the d_{14} element to be non-zero:

$$d_{il} = \begin{pmatrix} 0 & 0 & 0 & d_{14} & 0 & 0 \\ 0 & 0 & 0 & 0 & d_{14} & 0 \\ 0 & 0 & 0 & 0 & 0 & d_{14} \end{pmatrix} \quad (1.21)$$

This material's properties can be engineered by realizing an alloy with AlAs, obtaining $\text{Al}_x\text{Ga}_{1-x}\text{As}$ with different molar concentration x , as shown in Figure 4.

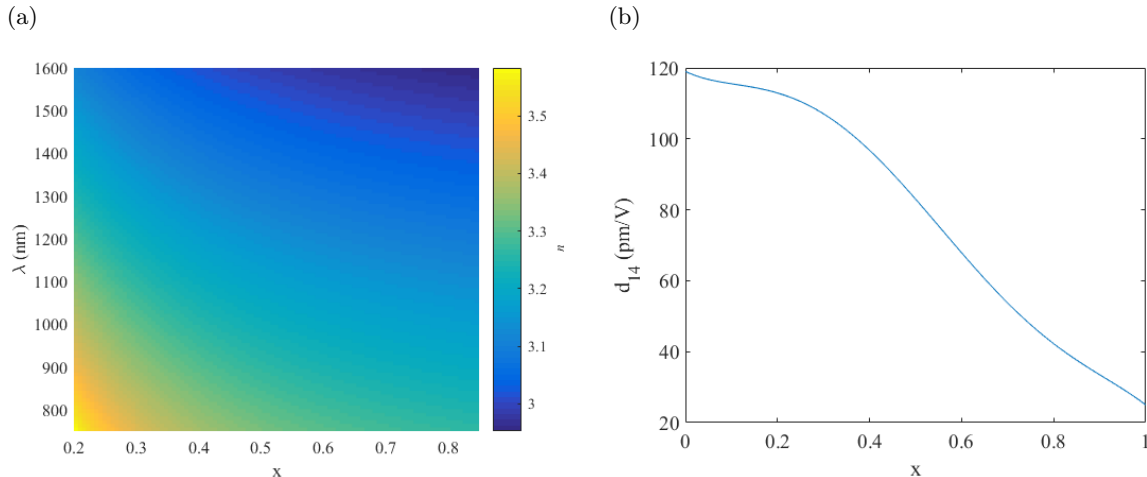


Figure 4: $\text{Al}_x\text{Ga}_{1-x}\text{As}$ properties as a function of molar concentration: (a) refractive index n , calculated with Gerhsitz model [18] (b) Second order non-linear coefficient d_{14} calculated using Ohashi model [19]

However, AlGaAs is isotropic, hence birefringent phase matching is not possible. QPM can be implemented through periodical poling by wafer bonding [20] or epitaxial regrowth [21], but this approach introduces significant losses. Our group works on integrated waveguide sources exploiting two types of QPM schemes:

- A source based on a copropagating phase matching scheme, where the pump, signal and idler fields all propagate along the direction of the waveguide, as sketched in figure 5a. This source uses *modal phase matching*, i.e. it exploits the difference in the effective refractive index of different types of guided modes;
- A source based on a counterpropagating phase matching scheme, sketched in 5b, where the pump impinges on the top of the waveguide and the signal and idler propagate in opposite directions along the waveguide. The phase matching scheme integrated by this source, on which I worked on during my internship, is detailed in the next section.

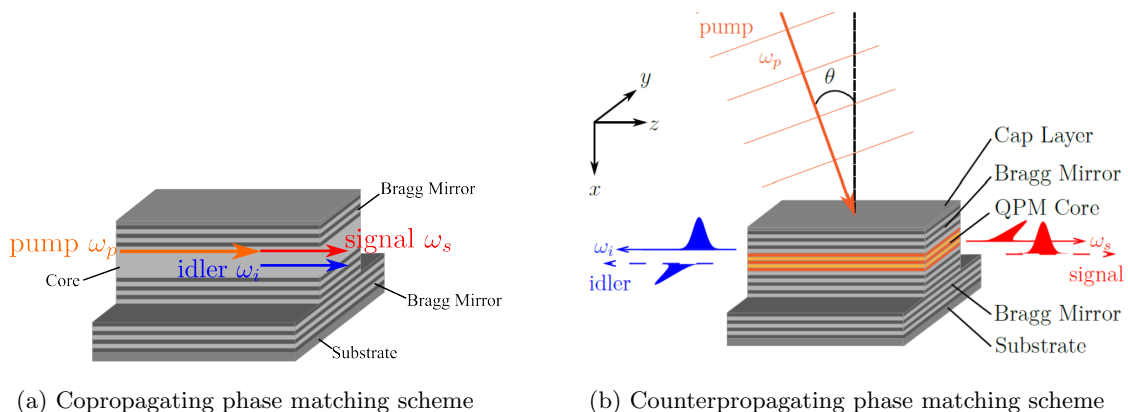


Figure 5: Sketches of the two different types of sources

2 Design of the counterpropagating source

The facet reflectivity has a very strong impact on the spectrum of the biphoton state emitted by the waveguide; in particular, increasing the reflectivity through the deposition of Bragg mirrors will allow us to achieve the spectral narrowing previously mentioned in the introduction. In this section, I present the results of my numerical simulations concerning the dimensions of the waveguide and the effect of the mirror deposition on both the facet reflectivity and the emitted biphoton state.

2.1 Dimensioning of the waveguide

Starting from a pre-existing epitaxial structure, I performed numerical simulations to choose the top width and the etching depth of the waveguide: the objective is to obtain signal and idler modes well confined in the structure and far from the flanks so that, when mirrors will be deposited, possible defects and imperfections induced by the deposition will not alter the fields in a significant way. The source consists of a ridge waveguide made of a stack of AlGaAs layers implementing the counter-propagating SPDC scheme. The Al concentration and thickness of each layer are displayed in Table 1. The cladding consists of a series of Bragg mirrors made of AlGaAs layers with 90% and 35% Aluminium content; these layers have three main functions [22]:

1. Confine the generated photons (at wavelength $\lambda = 1550$ nm) by total internal reflection
2. Create a resonant microcavity for the pump laser (at wavelength $\lambda = 775$ nm)
3. The bottom mirror avoids the penetration of the pump field into the substrate

The core instead consists of layers of 25% and 85% Al concentration, leading to an alternation of high and low $\chi^{(2)}$ value. This choice allows to implement a QPM scheme along the vertical direction: as pointed out in [23], the conversion efficiency depends on the *nonlinear overlap integral*:

$$\chi_{\Gamma} = \int d_{eff}(x)\Psi_P(x)\Phi_S(x)\Phi_I(x)dx \quad (2.1)$$

where Ψ_P , Φ_S and Φ_I are, respectively, the pump, signal and idler amplitude. Being inside a resonant microcavity, the pump is a stationary wave; in an homogeneous material, the positive and negative half-periods of this stationary wave would compensate each other and interfere destructively, giving $\chi_{\Gamma} = 0$. Instead, the structure is engineered in a way that the positive half-periods of the wave are in the high $\chi^{(2)}$ region and the negative half-periods are in correspondence of the low $\chi^{(2)}$ region, as it is represented in Figure 6 (reproduced from [23]): in this way, the contribution of the latter to the integral is attenuated, obtaining an overall positive χ_{Γ} . The spatial distribution of the modes for the final structure and the respective simulation results are reported, respectively, in Fig. 7 and Table 2. In the following, TE mode will also be referred as H polarization and TM as V polarization.

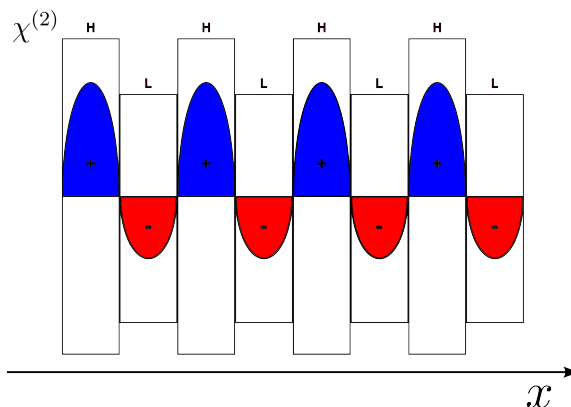


Figure 6: Representation of vertical QPM scheme. H and L correspond, respectively, to high and low $\chi^{(2)}$ regions. Reproduced from [23]

Number of periods	Role	Al content (%)	Thickness h (nm)
1	Substrate	0	
36	Bottom Bragg	90	70.8
		35	50.1
1	Buffer	90	125.1
4	Core	25	129.1
		80	104.3
1	Core	25	129.1
1	Buffer	90	125.1
14	Top Bragg	35	50.1
		90	70.8
1	Cap	0	50.0

Table 1: Epitaxial structure of wafer K7AD121

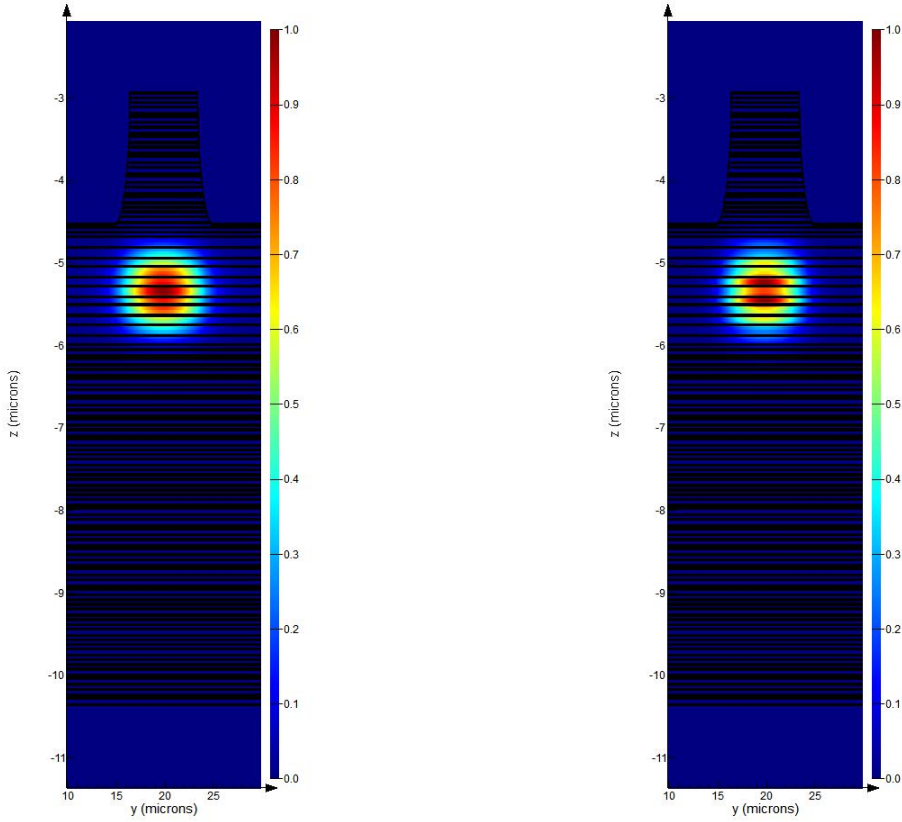


Figure 7: Left: TE mode spatial distribution. Right: TM mode spatial distribution

Top width		$7 \mu m$
Etch depth		$1.6 \mu m$
	n_{eff} at $\lambda = 1550$ nm	confinement
TE	3.087435	90.00%
TM	3.073054	94.17%

Table 2: Effective refractive index and confinement factor for the waveguide reported in Fig. 7

In a counterpropagating geometry (see sketch shown in Figure 8), the energy conservation and phase matching conditions:

$$\begin{cases} \omega_p = \omega_s + \omega_i \\ \mathbf{k}_p = \mathbf{k}_s + \mathbf{k}_i \end{cases} \quad (2.2)$$

can be rewritten as:

$$\begin{cases} \omega_p = \omega_s + \omega_i \\ \frac{\omega_p}{c} \sin \theta = k_s - k_i \\ \frac{n_p(\omega_p, x)\omega_p}{c} \cos \theta = k_{QPM} \end{cases} \quad (2.3)$$

The third equation describes how the vertical component of the pump wavevector is compensated by the QPM scheme. The second equation highlights one of the key features of the source, its tunability: by changing the angle with which the pump field impinges on top of the waveguide, it is possible to tune the wavelength of the emitted photons.

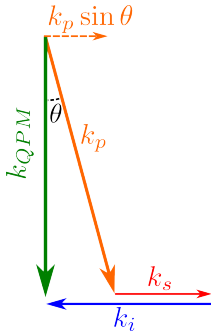


Figure 8: Counter propagating phase matching scheme. Reproduced from [22].

2.2 Study of the effect of mirror deposition on the facets reflectivity

In this section, I report the numerical study I did on the effect of the Bragg mirror deposition on the facets modal reflectivity. At first I used a plane wave approximation, then I refined the simulation by using a Finite Difference Time Domain (FDTD) method.

In the plane wave approximation, we consider a plane wave with wavelength λ_B impinging on a mirror constituted of N bi-layers made of two materials of refractive index n_1, n_2 of optical thickness $\frac{\lambda_B}{4}$. The reflectivity at wavelength λ_B is given by [24]:

$$R = \left[\frac{1 - \frac{n_e}{n_i} \left(\frac{n_2}{n_1} \right)^{2N}}{1 + \frac{n_e}{n_i} \left(\frac{n_2}{n_1} \right)^{2N}} \right]^2 \quad (2.4)$$

where n_i and n_e are respectively the indexes of the incident and exiting medium. In our case, SiO₂ was used as material 1 ($n_1 = 1.444$) and TiO₂ as material 2 ($n_2 = 2.3$) at $\lambda_B = 1550$ nm, going from a guided mode in AlGaAs waveguide (modal effective index $n_i \simeq 3.1$) to air ($n_e = 1$). More accurate results can be obtained by performing a Finite Difference Time Domain (FDTD) simulation: this method discretizes and numerically solves the time-dependent Maxwell equations in a finite spatial and temporal grid for an arbitrary source, overcoming the plane wave approximation. Results obtained using the two approaches are reported in Table 3 and 4.

	N = 1	N = 2	N = 3	N = 4	N = 5	N = 6
R	59.97%	81.82%	92.40%	96.93%	98.78%	99.52%

Table 3: Simulated reflectivity values obtained using Equation 2.4

	N = 0	N = 1	N = 2	N = 3	N = 4	N = 5	N = 6
R (TE)	29.56%	63.01%	83.77%	92.24%	96.62%	98.32%	98.98%
R (TM)	22.87%	55.02%	77.72%	87.5%	92.95%	95.42%	96.74%

Table 4: Simulated reflectivity values obtained by FDTD simulations of our waveguide

These values of reflectivity can in turn be used to calculate the Fabry-Pérot transmission spectra

displayed in Fig. 9 according to [25]:

$$T = \left(1 + \frac{4R}{(1-R)^2} \sin^2 \frac{\delta}{2} \right)^{-1} \quad (2.5)$$

where $\delta = \frac{2\pi\Delta}{\lambda}$, $\Delta = 2nL$, n is the modal effective refractive index and L is the mirror distance (i.e. the waveguide length). Because of the birefringence of the waveguide, the TE transmission spectrum T_{TE} and the TM transmission spectrum T_{TM} are not perfectly superimposed. In order to quantify the degree of overlap, we use the quantity:

$$\frac{\int T_{TE}(\lambda) \cdot T_{TM}(\lambda) d\lambda}{\sqrt{\int T_{TE}^2(\lambda) d\lambda \cdot \int T_{TM}^2(\lambda) d\lambda}} \quad (2.6)$$

If the number of mirrors increases, the reflectivity increases, so the peaks become narrower and the overlap decreases; this can represent a problem in case we want to dispose of indistinguishable photons, a useful resource for a variety of quantum protocols. In order to counter this behaviour, we can imagine to compensate the birefringence of the structure by acting e.g. on temperature, strain or by using the electro-optic effect. This would enable to tune the resonance frequencies of TE and TM photon, increasing their overlap, as shown in Figure 10. In this way, the overlap is limited only by the different reflectivity of the two modes. A comparison between overlap values before and after this correction is listed in Table 5.

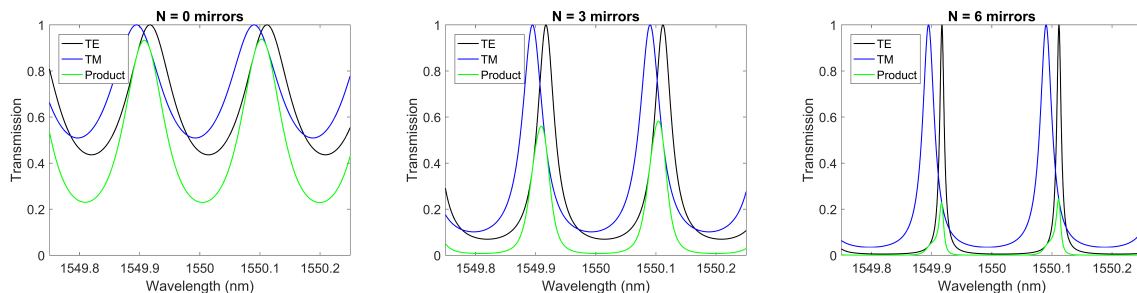


Figure 9: Fabry-Pérot spectra obtained from Eq. 2.5

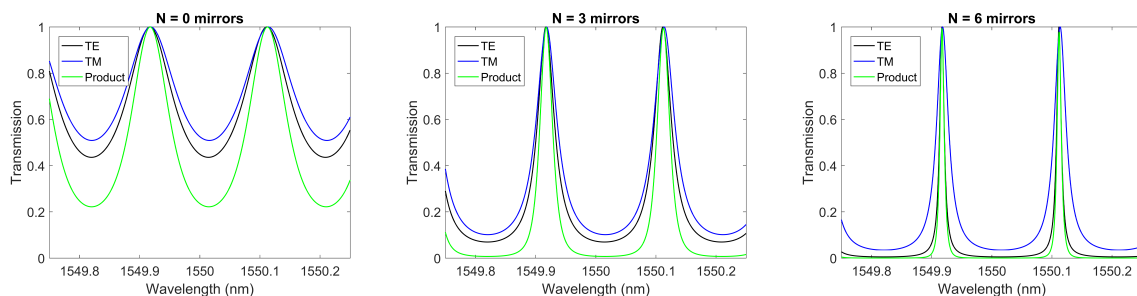


Figure 10: Fabry-Pérot spectra obtained from Eq. 2.5 after birefringence compensation

	N = 0	N = 1	N = 2	N = 3	N = 4	N = 5	N = 6
With birefringence	0.9814	0.9408	0.8676	0.7716	0.6636	0.5595	0.3270
Without birefringence	0.9985	0.9974	0.9954	0.9920	0.9872	0.9845	0.8788

Table 5: Overlap values

2.3 Joint Spectral Amplitude

In this section I describe the calculations of the quantum properties of the state emitted by the waveguide I have designed. Let us consider the down conversion of a pump field $E_p(\omega_p)$ in an H -polarized signal

photon and a V -polarized idler (HV interaction for short)¹, that are respectively in the guided modes $E_s(\omega_s)$ and $E_i(\omega_i)$. As depicted in Figure 5b, we call signal the photon propagating to the right and idler the one propagating to the left. The emitted biphoton state can be written as [22]:

$$|\psi\rangle = \iint d\omega_s d\omega_i \phi(\omega_s, \omega_i) \hat{a}_H^\dagger(\omega_s) \hat{a}_V^\dagger(\omega_i) |0\rangle \quad (2.7)$$

where $\hat{a}_\sigma^\dagger(\omega)$ are the creation operators for a photon with polarization σ and frequency ω and $\phi(\omega_s, \omega_i)$ is the Joint Spectral Amplitude (JSA):

$$\begin{aligned} \phi(\omega_s, \omega_i) &= \frac{\epsilon_0 L}{i\beta\hbar\sqrt{v_g^H(\omega_s)v_g^V(\omega_i)}} \\ &\times \int d\mathbf{r} \chi^{(2)} E_p(\mathbf{r}, \omega_s + \omega_i) E_H(x, y, \omega_s) E_V(x, y, \omega_i) e^{-i\Delta k z} \end{aligned} \quad (2.8)$$

$v_g^\sigma(\omega)$ are the group velocities, L is the waveguide length and β is the generation probability. The JSA normalization reads:

$$\langle\psi|\psi\rangle = \iint d\omega_s d\omega_i |\phi(\omega_s, \omega_i)|^2 = 1 \quad (2.9)$$

The squared modulus of the JSA, called Joint Spectral Intensity (JSI), corresponds to the probability to find a pair of photons with respective frequencies ω_s and ω_i . The JSA can be factorized as:

$$\boxed{\phi(\omega_s, \omega_i) = \chi_\Gamma(\omega_s, \omega_i) \cdot \text{PM}(\omega_s, \omega_i) \cdot \phi_{\text{spectral}}(\omega_s, \omega_i)} \quad (2.10)$$

The factor χ_Γ is the overlap integral between the fields:

$$\begin{aligned} \chi_\Gamma &= \frac{\epsilon_0 L \epsilon_p^{(0)}}{i\beta\hbar\sqrt{v_g^H(\omega_s)v_g^V(\omega_i)}} \\ &\times \iint dx dy \chi^{(2)}(x) \Pi_W(y) f_{\mu\text{cavity}}(x) \phi_p(y) E_H(x, y, \omega_s) E_V(x, y, \omega_i) \end{aligned} \quad (2.11)$$

where $\epsilon_p^{(0)}$ is a normalization constant, $f_{\mu\text{cavity}}(x)$ describes the effect of the vertical microcavity, $\phi_p(y)$ is the pump transverse spatial profile along the y direction and

$$\Pi_W(y) = \begin{cases} 1 & \text{if } |y| < \frac{L}{2} \\ 0 & \text{otherwise} \end{cases} \quad (2.12)$$

takes into account the finite size of the sample. The second factor $\text{PM}(\omega_s, \omega_i)$ in Equation 2.10 describes the phase matching condition:

$$\text{PM}(\omega_s, \omega_i) = \int dz \Pi_L(z) \phi_p(z, \omega_+) e^{-ik_{deg}(\omega_+)z - i\frac{\omega_-}{\bar{v}_g}z} \quad (2.13)$$

where $\omega_- = \omega_s - \omega_i$; $\phi_p(z, \omega_+)$ contains the dependence of the pump's transverse spatial profile on z and on $\omega_+ = \omega_s + \omega_i = \omega_p$. k_{deg} is the value that the z -axis projection of the pump's wavevector should have to generate frequency-degenerate signal/idler pairs and it is linked to the device's birefringence according to:

$$k_{deg}(\omega_p) = \frac{\omega_p}{c} \frac{n_s - n_i}{2} = \frac{\omega_p}{c} \sin \theta_{deg} \quad (2.14)$$

\bar{v}_g is the average group velocity of the guided modes:

$$\bar{v}_g^{-1} = \left(\frac{v_g^H + v_g^V}{2} \right)^{-1} \quad (2.15)$$

and

$$\Pi_L(z) = \begin{cases} 1 & \text{if } |z| < \frac{W}{2} \\ 0 & \text{otherwise} \end{cases} \quad (2.16)$$

¹The same reasoning can be applied to the VH (i.e. V -polarized signal and H -polarized idler) interaction.

with W being the waveguide's width. Finally, the factor ϕ_{spectral} in Equation 2.10 takes into account the pump's energy spectrum and the vertical microcavity spectral effect:

$$\phi_{\text{spectral}} = f_{\text{spectrum}}(\omega_+) f_{\text{mcav}}(\omega_+) \quad (2.17)$$

Equation 2.13 highlights the impact of the pump beam profile on the JSA: for instance, Figure 11 shows the effect of the waist size of a Gaussian pump beam on the JSI: the width of the JSI along the anti-diagonal in the (λ_s, λ_i) plane is inversely proportional to the waist size. In a previous work of the QITE team it was shown that, through pump beam shaping techniques, it is possible to control the exchange statistics in frequency of the generated photon pairs, obtaining fermionic [22] [26] and anyonic behaviour [27].

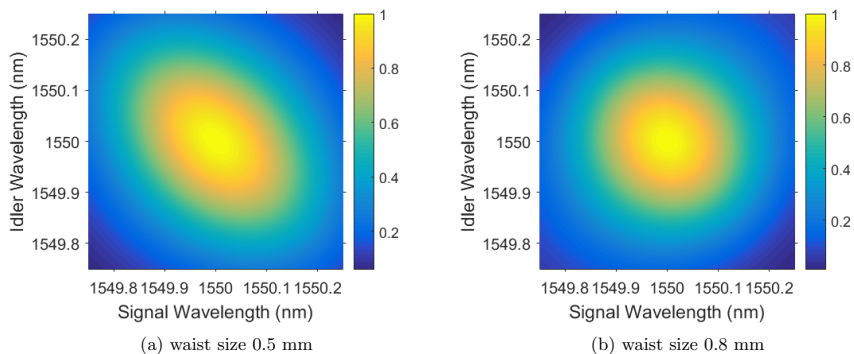


Figure 11: Simulations of the JSI for a Gaussian pump beam having different waist size

2.4 Fabry-Pérot cavity effect

In this section we show the effect of the facets reflectivity on the Joint Spectral Amplitude. The role of facet reflectivity in the process of SPDC was first analysed by Jeronimo-Moreno et al. [28]. G. Boucher and S. Francesconi applied their approach to the counterpropagating source [29] [22]. The basic idea is the following: assume a photon pair is generated at the center of the waveguide, with the signal photon propagating to the right and the idler going to the left. When the signal photon (with polarization σ) reaches the facet, it will be transmitted and exit on the right (\mathcal{R}) with probability $f_{t,\sigma}$ or it will be reflected back and exit on the left (\mathcal{L}) with probability $f_{r,\sigma}$; the mirror reasoning is valid for the idler photon. This effect can be taken into account by replacing the creation operators with the following expressions:

$$\hat{a}_{s,\sigma}^\dagger(\omega) \rightarrow f_{t,\sigma}(\omega) \hat{a}_{\mathcal{R},\sigma}^\dagger(\omega) + f_{r,\sigma}(\omega) \hat{a}_{\mathcal{L},\sigma}^\dagger(\omega) \quad (2.18a)$$

$$\hat{a}_{i,\sigma}^\dagger(\omega) \rightarrow f_{t,\sigma}(\omega) \hat{a}_{\mathcal{L},\sigma}^\dagger(\omega) + f_{r,\sigma}(\omega) \hat{a}_{\mathcal{R},\sigma}^\dagger(\omega) \quad (2.18b)$$

The transmission and reflection probabilities are given by the Fabry-Pérot cavity functions:

$$f_{t,\sigma}(\omega) = \frac{\sqrt{1 - R_\sigma} e^{i \frac{\omega n L}{2c}}}{1 - R_\sigma e^{i \frac{2\omega n L}{c}}} \quad (2.19a)$$

$$f_{r,\sigma}(\omega) = \frac{\sqrt{R_\sigma (1 - R_\sigma)} e^{i \frac{3\omega n L}{2c}}}{1 - R_\sigma e^{i \frac{2\omega n L}{c}}} \quad (2.19b)$$

where R_σ are the modal reflectivities. As a consequence, there is a non-zero probability to have both photons exiting on the same side, or a signal photon exiting on the left and an idler exiting on the right; in order to select an HV interaction (that is an H -polarized signal photon at frequency ω_s on the right side and a V -polarized idler with frequency ω_i on the left), we put a polarizer and a frequency filter at each output of the device, reducing Equations 2.18a and 2.18b to:

$$\hat{a}_{s,H}^\dagger(\omega_s) \rightarrow f_{t,H}(\omega_s) \hat{a}_{s,H}^\dagger(\omega_s) \quad (2.20a)$$

$$\hat{a}_{i,V}^\dagger(\omega_i) \rightarrow f_{t,V}(\omega_i) \hat{a}_{i,V}^\dagger(\omega_i) \quad (2.20b)$$

Therefore, the final result is a multiplication of the original JSA of Equation 2.10 by the two Fabry-Pérot functions:

$$\boxed{\phi_{FP}(\omega_s, \omega_i) = \phi(\omega_s, \omega_i) \cdot f_{t,H}(\omega_s) \cdot f_{t,V}(\omega_i)} \quad (2.21)$$

As shown by Figures 13b and 13c, this gives the JSI a chessboard-like pattern governed by the position and the width of the Fabry-Pérot peaks (the first determined by the modal refractive index n_σ and the second by the modal reflectivity R_σ).

2.5 Hong-Ou-Mandel interference in the single interaction case

In this section I describe the Hong-Ou-Mandel interference and I analyze the impact of the facets reflectivity on the interferogram. The Hong-Ou-Mandel (HOM) experiment [30] is an interference setup that allows to assess the indistinguishability of photon pairs, a widely used resource in quantum information protocols. The setup is illustrated in Figure 12: two independent and indistinguishable photons enter a 50:50 beamsplitter from the input ports 1 and 2; port 2 is also equipped with a delay line τ . At the output ports 3 and 4 there are two Single Photon Detectors, in turn connected to a coincidence counter. Let us consider for now the case $\tau = 0$: using \hat{a}_i^\dagger for the creation operator and $|n\rangle_i$ for the number state n at port i , the input wavefunction is:

$$|\Psi\rangle_{in} = |1\rangle_1 |1\rangle_2 = \hat{a}_1^\dagger \hat{a}_2^\dagger |0\rangle \quad (2.22)$$

where $|0\rangle$ is the vacuum state. The effect of the beamsplitter consists in the substitution [31]:

$$\begin{aligned} \hat{a}_1^\dagger &\rightarrow \frac{1}{\sqrt{2}} (\hat{a}_3^\dagger + \hat{a}_4^\dagger) \\ \hat{a}_2^\dagger &\rightarrow \frac{1}{\sqrt{2}} (\hat{a}_3^\dagger - \hat{a}_4^\dagger) \end{aligned} \quad (2.23)$$

Hence at the output we get:

$$\begin{aligned} |\Psi\rangle_{out} &= \frac{1}{2} (\hat{a}_3^\dagger + \hat{a}_4^\dagger) (\hat{a}_3^\dagger - \hat{a}_4^\dagger) |0\rangle = \\ &= \frac{1}{2} (\hat{a}_3^{\dagger 2} - \cancel{\hat{a}_3^\dagger \hat{a}_4^\dagger} + \cancel{\hat{a}_4^\dagger \hat{a}_3^\dagger} - \hat{a}_4^{\dagger 2}) |0\rangle = \\ &= \frac{1}{\sqrt{2}} (|2\rangle_3 |0\rangle_4 - |0\rangle_3 |2\rangle_4) \end{aligned} \quad (2.24)$$

The simplification on the second line was possible because \hat{a}_3^\dagger and \hat{a}_4^\dagger commute. In conclusion, if the photons are indistinguishable, they both exit from the same output port and no coincidences are registered by the counter. If $\tau \neq 0$, the photons arrive at different times, lose their indistinguishability and the coincidence rate gradually reaches the value 0.5; the final result is a characteristic Hong-Ou-Mandel dip. This is valid for two independent photons: in the case of our biphoton state, the two photons must be treated as a whole and it can be proven that the coincidence probability for a temporal delay τ is [22]:

$$P_c(\tau) = \frac{1}{2} - \frac{1}{2} \text{Re} \left[\iint d\omega_3 d\omega_4 \phi^*(\omega_4, \omega_3) \phi(\omega_3, \omega_4) e^{i(\omega_4 - \omega_3)\tau} \right] \quad (2.25)$$

Therefore, a sufficient and necessary condition to have no coincidences at $\tau = 0$ is to dispose of photon pairs with a symmetric JSA in the frequency domain:

$$\phi(\omega_3, \omega_4) = \phi(\omega_4, \omega_3) \quad (2.26)$$

In Figures 13 I show the results of my JSI simulations with the respective HOM interferograms calculated according to Equation 2.25. Two important aspects can be deduced from them:

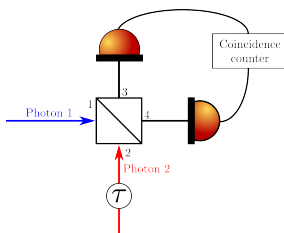


Figure 12: HOM setup

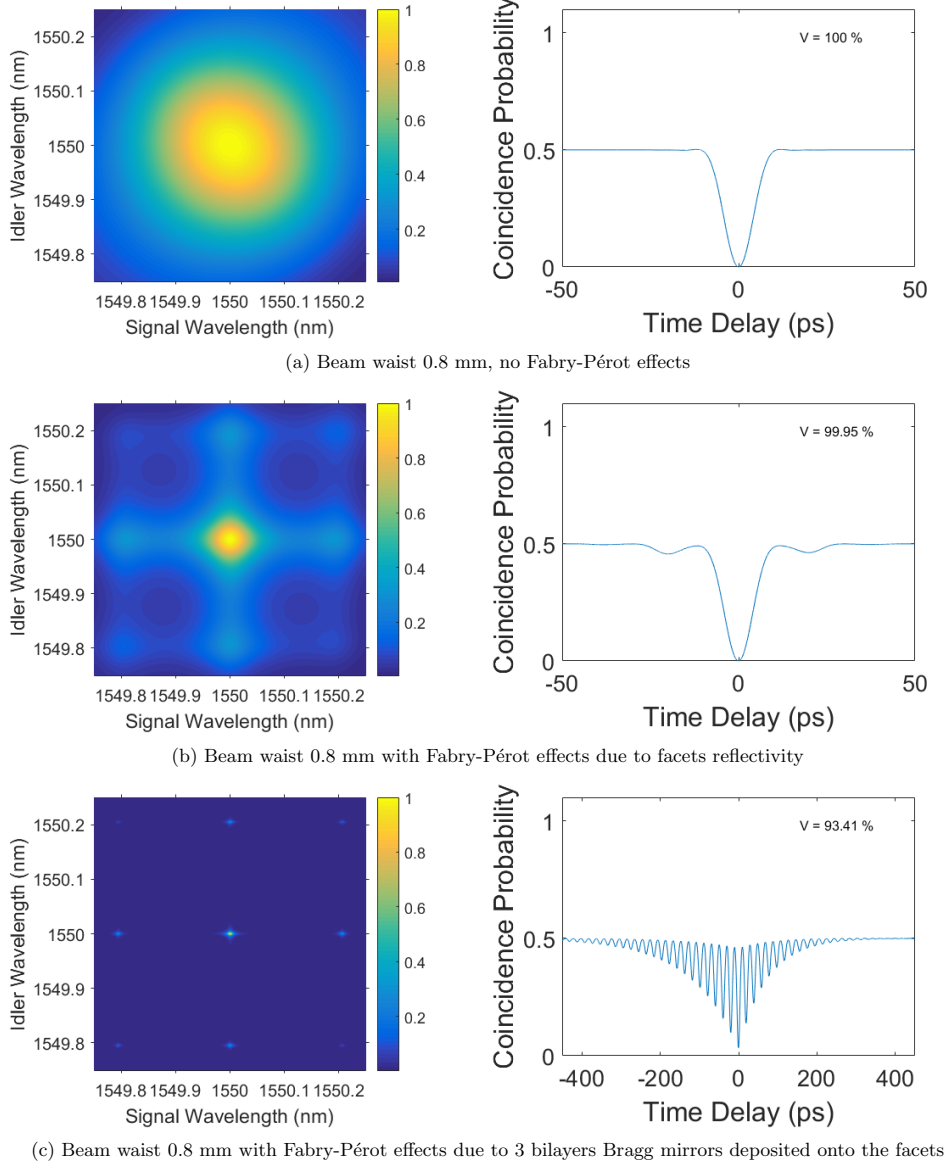


Figure 13: Examples of JSIs and their relative HOM graphs for three different situations of reflectivity

1) Interferograms 13b and 13c present satellites dips at delay times τ equal to integer multiples of the cavity round trip time τ_{RT} . This is due to the presence of the cavity, which allows a photon that exits the waveguide at time $t=0$ to interfere with a photon that exits after one (or multiple) round trips. Hence, higher reflectivity means that a photon can do many more round trips before exiting, enhancing this effect and producing more dips. Moreover, the interferogram in Figure 13c is not symmetric because of the difference in the facets modal reflectivity;

2) Interferogram 13c has a dip visibility V lower than 100%, indicating partial distinguishability. Indeed, $n_{TE} \neq n_{TM}$ and $R_{TE} \neq R_{TM}$, so the Fabry-Pérot spectra of signal and idler are slightly different, decreasing the degree of indistinguishability of the two photons. In particular, further simulations show that:

- if $n_{TE} = n_{TM}$ and $R_{TE} = R_{TM}$, $V = 100\%$
- if $n_{TE} \neq n_{TM}$ and $R_{TE} = R_{TM}$, $V = 98.98\%$
- if $n_{TE} = n_{TM}$ and $R_{TE} \neq R_{TM}$, $V = 94.04\%$
- if $n_{TE} \neq n_{TM}$ and $R_{TE} \neq R_{TM}$, $V = 93\%$

Hence, the difference in reflectivity plays a more important role in distinguishability than the waveguide birefringence.

There is a way to eliminate the birefringence of the waveguide, as it will be detailed in the following.

2.6 Hong-Ou-Mandel interference in the double interaction case

In this section I report the results of the numerical study of the effect of the facets reflectivity on the HOM interferogram when taking into account the two possible generation processes occurring in the device. As specified at the beginning of the chapter, so far we considered the case of a single interaction (HV), which can be achieved by the use of polarizers and filters. On the other hand, if we keep both interactions, the emitted state can be written as [22]:

$$|\Psi\rangle = \iint d\omega_1 d\omega_2 \left[\phi_{VH}(\omega_1, \omega_2) \hat{a}_{s,V}^\dagger(\omega_1) \hat{a}_{i,H}^\dagger(\omega_2) + \phi_{HV}(\omega_1, \omega_2) \hat{a}_{s,H}^\dagger(\omega_1) \hat{a}_{i,V}^\dagger(\omega_2) \right] |0\rangle \quad (2.27)$$

where ϕ_{HV} and ϕ_{VH} are, respectively, the JSA of the HV and VH interaction, with the normalization condition:

$$\iint d\omega_1 d\omega_2 \left[|\phi_{HV}(\omega_1, \omega_2)|^2 + |\phi_{VH}(\omega_1, \omega_2)|^2 \right] = 1 \quad (2.28)$$

This kind of interaction allows to obtain Hybrid Polarization Frequency (HPF) entangled states: if the frequency modes are well separated, we can approximate the JSAs with Dirac deltas ($\phi(\omega_1, \omega_2) \sim \delta(\omega_1 - \omega_1^0)\delta(\omega_2 - \omega_2^0)$), thus getting:

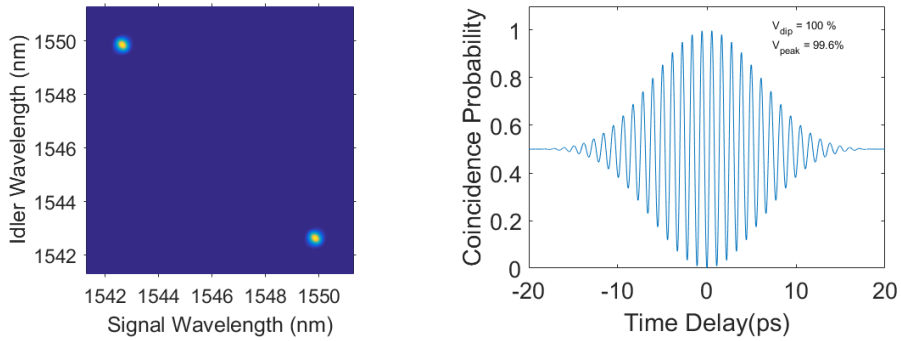
$$|\Psi\rangle \sim |V, \omega_1^0\rangle_s |H, \omega_2^0\rangle_i + |H, \omega_2^0\rangle_s |V, \omega_1^0\rangle_i \quad (2.29)$$

which is an entangled state in the hybrid polarization/frequency space in the basis $\{|V, \omega_1^0\rangle, |H, \omega_2^0\rangle\}$.

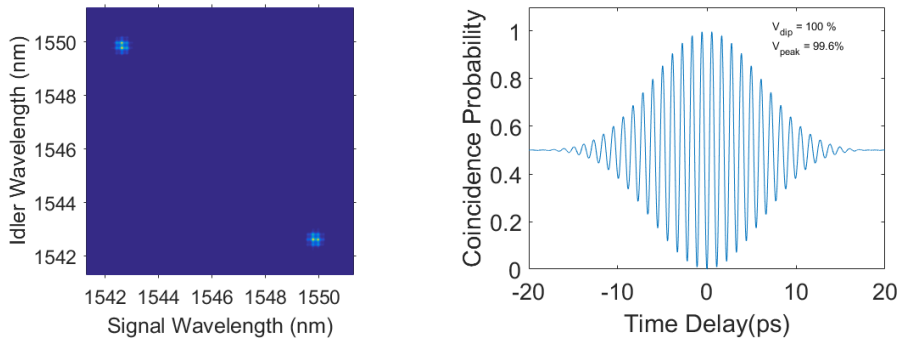
As in the single interaction case, it is possible to calculate the HOM interferogram:

$$P_c(\tau) = \frac{1}{2} - \text{Re} \left[\iint d\omega_3 d\omega_4 \phi_{VH}^*(\omega_4, \omega_3) \phi_{HV}(\omega_3, \omega_4) e^{-i(\omega_4 - \omega_3)\tau} \right] \quad (2.30)$$

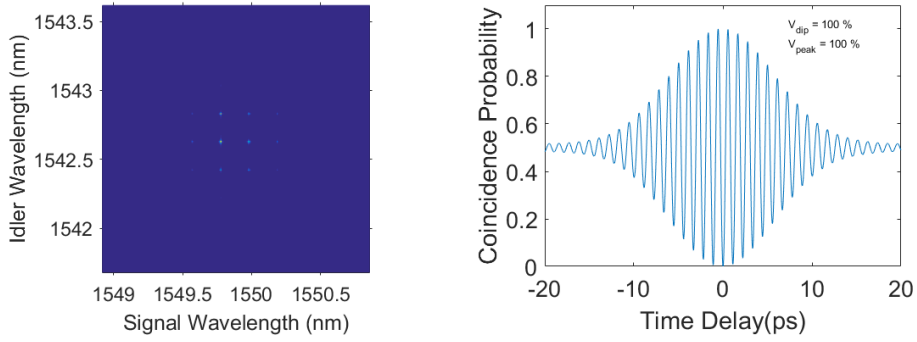
Figures 14 show the simulations of the JSI and the respective HOM interferogram, which, for this kind of biphoton state, is characterized by the presence of both a dip and a peak. It is worth noticing that the dip visibility is not affected by the Fabry-Pérot effects (i.e. by the birefringence and the difference in modal reflectivity): this can be explained by the fact that this state contains the sum of the HV and VH interaction, compensating these differences. The distance between the two lobes that are present in the JSI is governed by the birefringence: the larger Δn is, the further they are from each other; in the case of a non-birefringent waveguide, the two lobes collapse in one and the same HOM interferogram of a single interaction picture is obtained.



(a) Beam waist 0.8 mm, no Fabry-Pérot effects



(b) Beam waist 0.8 mm with Fabry-Pérot effects due to facets reflectivity



(c) Beam waist 0.8 mm with Fabry-Pérot effects due to 3 bilayers Bragg mirrors deposited onto the facets; JSI is zoomed in one of the lobes

Figure 14: Examples of JSIs and their relative HOM graphs for three different situations of reflectivity

2.7 Dry etched waveguide

The dependence of the modal refractive indexes on the waveguide width was pointed out in S. Francesconi's PhD thesis [22]. In order to exploit this dependence to eliminate the birefringence, however, the waveguide width must be slightly above $1 \mu\text{m}$; such dimensions cannot be achieved using UV lithography and wet etching, but require e-beam lithography and dry etching, enabling the fabrication of a waveguide with steep vertical sidewalls. Comparison between the two etching profiles can be seen in the SEM images in Figure 15 [22].

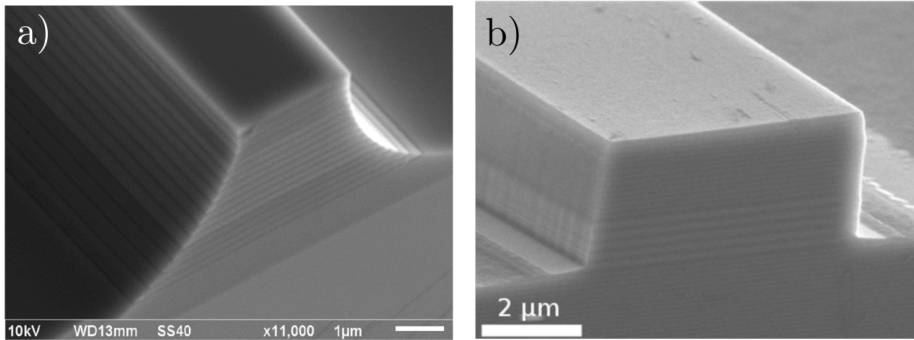


Figure 15: Comparison between a wet etched waveguide profile (a) and a dry etched waveguide profile (b)

Figure 16 depicts the difference Δn between the modal refractive indexes of the TE and TM polarized modes generated by SPDC as a function of the waveguide width. The condition $\Delta n = 0$ is met for a width of $1.18 \mu\text{m}$; the corresponding spatial profiles of the two modes are shown in Figure 17. Since the other distinguishability source is the difference in modal reflectivity, I also performed the reflectivity FDTD simulation for this waveguide, obtaining the results reported in Table 6. These simulations show that, unlike the wet etched waveguide, the dry etched sample's reflectivity saturates around 90%.

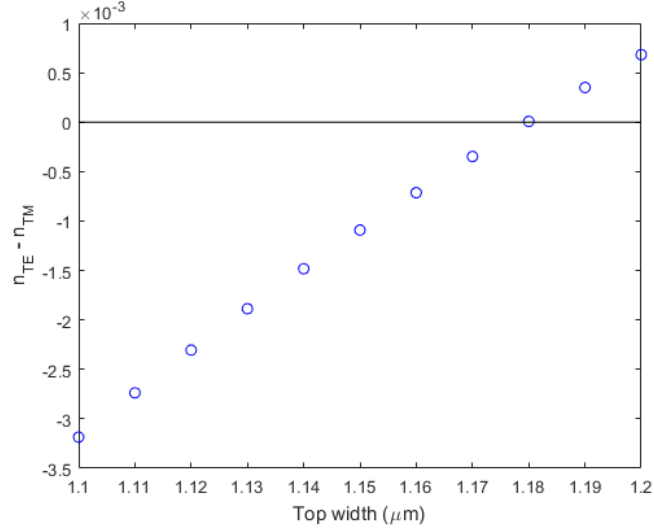


Figure 16: Birefringence as a function of waveguide's width

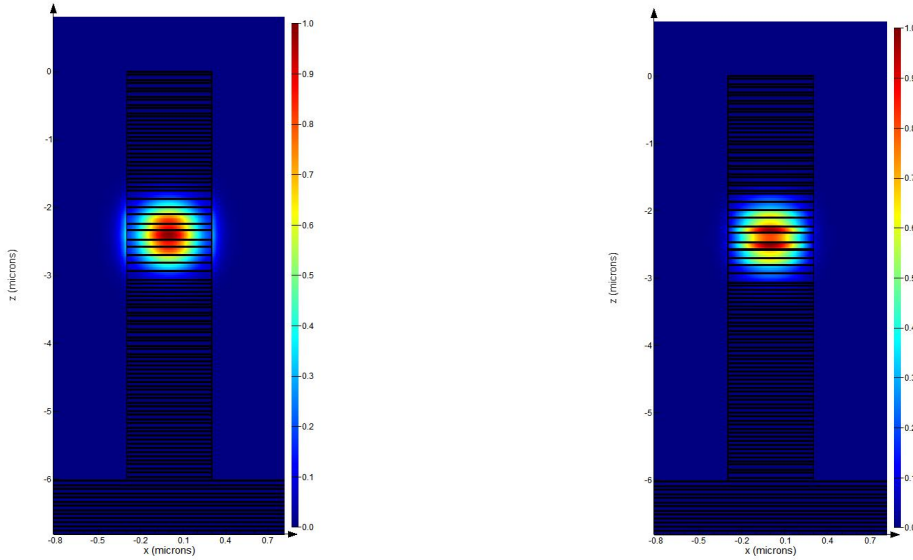


Figure 17: Spatial distribution of the modes in 1.18 μm -wide dry etched waveguide. Left: TE polarization. Right: TM polarization

	N=0	N=1	N=2	N=3	N=4	N=5	N=6
$R (TE)$	0.2907	0.5293	0.7092	0.7892	0.8397	0.8620	0.8708
$R (TM)$	0.3298	0.5958	0.7734	0.8447	0.8856	0.9012	0.9085

Table 6: Simulated reflectivity values obtained by FDTD of the 1.18 μm wide dry etched waveguide

In all the simulations, mirrors had an optical thickness of $\frac{\lambda}{4}$, a value that in theory should work with plane waves. Since the mode is propagating in such a narrow structure, the plane wave approximation may not work very well, so I slightly varied the thickness of the mirrors from this value to see if I could gain in reflectivity. However, the gain is very small: with mirrors 5% thicker, reflectivity increases only by around 1%.

To understand the reason behind this lower reflectivity, I performed other simulations varying the width of the waveguide. These simulations show that, when the waveguide width is below 2.5 μm , the field starts leaking out of the waveguide, probably due to diffraction effects. Figure 18 is the field distribution in a cross-section of the waveguide in a specific time-instant of the simulation, showing the field spreading outside of the waveguide edges (marked in black). In order to quantify this effect, a

confinement factor can be defined as:

$$C(t) = \frac{\iint_{guide} |\mathbf{E}(x, z, t)| dx dz}{\iint_{whole\ space} |\mathbf{E}(x, z, t)| dx dz} \quad (2.31)$$

where $\mathbf{E}(x, z, t)$ is the time-dependent field passing through the cross-section of the waveguide at each time instant of the simulation. The time-average value of this factor is 76.76% and 80.88% for the TE and TM modes respectively; its time evolution is shown in Figure 19. For reference, figure 20 shows the same parameter for the two modes mode in a 2.25 μm -wide waveguide; in this case, the average confinement is 98.52% and 96.76% for TE and TM mode respectively. The lower confinement of the 1.18 μm -wide waveguide may be the cause of the reflectivity saturation: since part of the field exits from the guide, it does not see the AlGaAs/mirror interface but the air/mirror interface and this, in turn, may limit the reflectivity. On the other hand, the Finite Difference Eigenmode (FDE) simulations that I used to calculate the eigenmodes in Figure 17 show that the confinement in the 1.18 μm -wide waveguide is around 90.5% of the TE polarization and around 96.6% for the TM polarization. The two simulation methods use different approaches: the FDTD discretizes and numerically solves the time-dependent Maxwell equations in a finite spatial and temporal grid for a given source, while FDE discretizes the 2D cross-section of the waveguide and solves the matrix eigenvalue problem to calculate the profile and effective refractive index of its eigenmodes. The incongruence between the results obtained via the two methods may indicate the presence of simulation artefacts; further simulations are required to clarify this aspect.

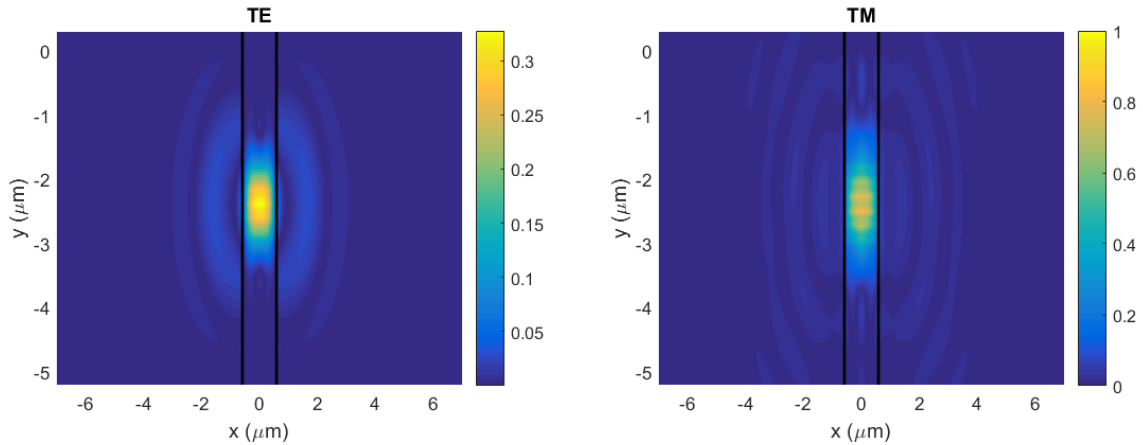


Figure 18: Time snapshot of TE (left) and TM (right) field distribution

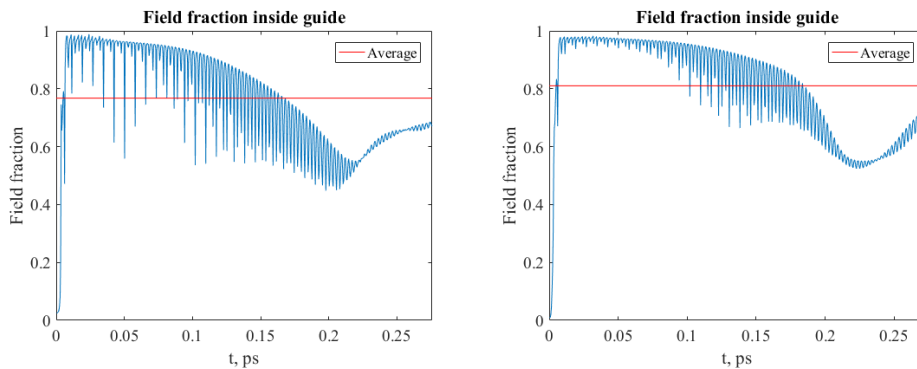


Figure 19: Field confinement of the TE (left) and TM (right) mode inside the 1.18 μm wide waveguide

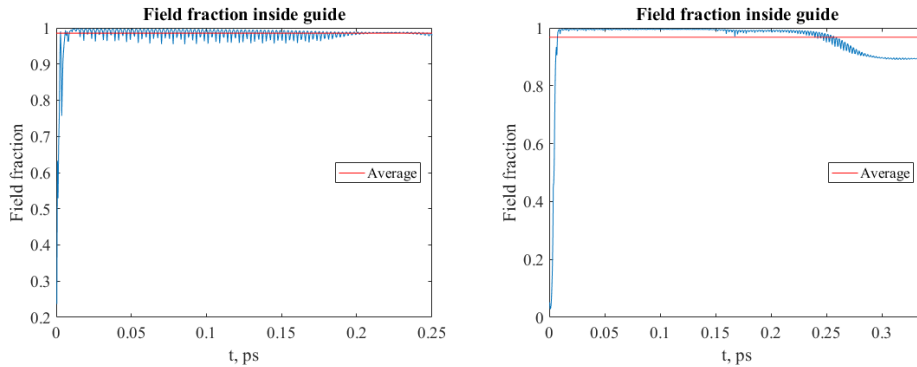


Figure 20: Field confinement of the TE (left) and TM (right) mode in a $2.25 \mu\text{m}$ wide waveguide

FDTD simulations also show that, even if the field does not stay strictly confined inside the $1.18 \mu\text{m}$ -wide waveguide, it still stays close to the waveguide's edges, getting around $3 \mu\text{m}$ far from them. Figure 21 shows the confinement factor in this region. If this is the case, a possibility to increase the confinement inside the guide could be surrounding it with some other structure to push the field back in. This idea will be further analyzed in my future PhD thesis work.

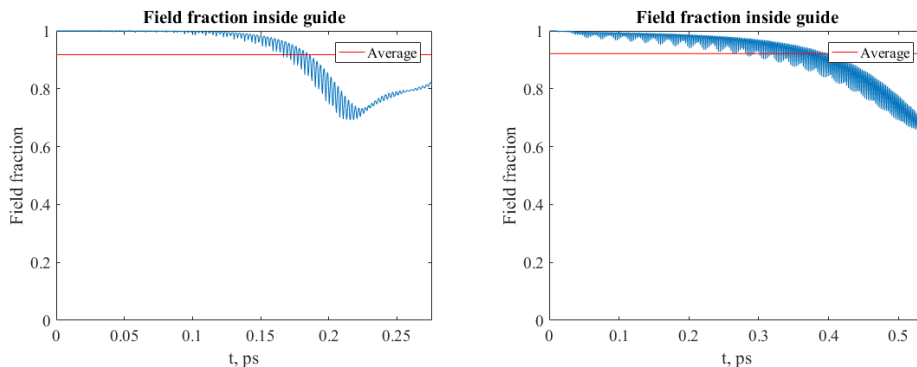


Figure 21: Field confinement of the TE (left) and TM (right) mode in a $3 \mu\text{m}$ region around the $1.18 \mu\text{m}$ wide waveguide

3 Fabrication and characterization of samples with high reflectivity mirrors

In this section I detail the fabrication and characterization of samples provided with high reflectivity Bragg mirrors. To perform the deposition, I participated to the discussion with X. Lafosse, engineer of the Center for Nanoscience and Nanotechnology (C2N), discussing with him about the choice of materials and number of mirrors. We came to the conclusion that 3 mirrors of $\text{SiO}_2/\text{TiO}_2$ bi-layers on each facet of the waveguide should give at the same time high reflectivity, good adhesion and a good general quality of the deposition. The discussion was supported by the numerical simulation I performed.

3.1 Deposition technique

SiO_2 and TiO_2 were deposited by X. Lafosse at C2N by Ion Beam Assisted Deposition (IBAD). In this technique, a material is evaporated by an electron beam and bombarded by low-energy ions. The ion beam is a widely used tool in micro and nanofabrication thanks to its flexibility and versatility: for instance, by changing ion species, beam shape and ion energy, one can achieve physical or chemical etching or deposition. IBAD is widely used for the deposition of optical dielectric films: when evaporated, hard materials such as TiO_2 , HfO_2 and fluorides tend to have low thermal energy and, when deposited, form a columnar microstructure [32], resulting in a low-density and porous film. During low-energy ion bombardment, knock-on target atoms can either leave the surface as sputtered atoms or be implanted below the surface and be trapped as interstitial atoms. The latter increases the local film density, while the voids left by sputtered atoms are filled by the e-beam evaporated atoms coming from the deposition source [33]. The final result is reduced porosity and increased film density.

Ti₃O₅ was used as starting material for the TiO₂ deposition because, when evaporated, TiO₂ stoichiometry changes, causing the physical and optical properties (in particular, the refractive index) of the final film to change in unexpected and non-reproducible ways. Ti₃O₅, on the other hand, is much less susceptible to stoichiometry shifts, allowing higher control on the deposited film properties [34]. O₂ ion beam was used for the IBAD.

SiO₂ was deposited starting from SiO₂ itself using an ion beam of Ar and O₂. The O₂ ion flux and concentration is a very important parameter during the deposition: while being evaporated by the e-beam, some SiO₂ molecules may lose one O atom, becoming SiO and causing a shift in the final refractive index. Interaction with the O₂ ions allows these molecules to “recover” the lost O atom, obtaining a more uniform SiO₂ deposition [35].

3.2 Measurement of Fabry P erot spectra before mirror deposition

The wafer **K7AD121** was already available and had been realized in 2020 by A.Lemaitre at C2N by Molecular Beam Epitaxy. UV lithography and wet etching were performed to obtain the waveguides I have designed and presented in section 2.1; the process is schematically described in Figure 22. The resulting sample, named **K7AD121-L1**, contains 40 groups of waveguides, each group in turn containing 3 waveguides of different widths: the bottom one (B) is 8 μm wide, the middle one (M) 7 μm and the top one (T) 6 μm. I measured the Fabry-P erot spectra of a set of waveguides to verify that the sample was in good condition and to be able to compare the modal reflectivity before and after the mirror deposition. Optical losses were evaluated via the Fabry-P erot technique [36]: a tunable telecom laser was injected onto the waveguide and the power at the output facet was collected and measured. The transmitted power as a function of the laser wavelength presents Fabry-P erot fringes due to facets reflectivity, with a contrast K given by:

$$K = \frac{I_{max} - I_{min}}{I_{max} + I_{min}} \quad (3.1)$$

related to the internal optical losses via:

$$\tilde{R} = Re^{-\alpha L} = \frac{1 - \sqrt{1 - K^2}}{K} \quad (3.2)$$

where R is the (lossless) reflectivity, α is the propagation loss coefficient and L the waveguide length. Using the value of R obtained from the 3D numerical simulations (detailed in section 2.2) and the value of \tilde{R} from the experimental measurements, the optical loss coefficient can be evaluated as:

$$\alpha = \frac{1}{L} \ln \left(\frac{R}{\tilde{R}} \right) \quad (3.3)$$

The obtained results for the best two waveguides of the sample are detailed in table 7. Figures 23 and 24 show the experimental Fabry-P erot spectra of guide 20B and 24M respectively.

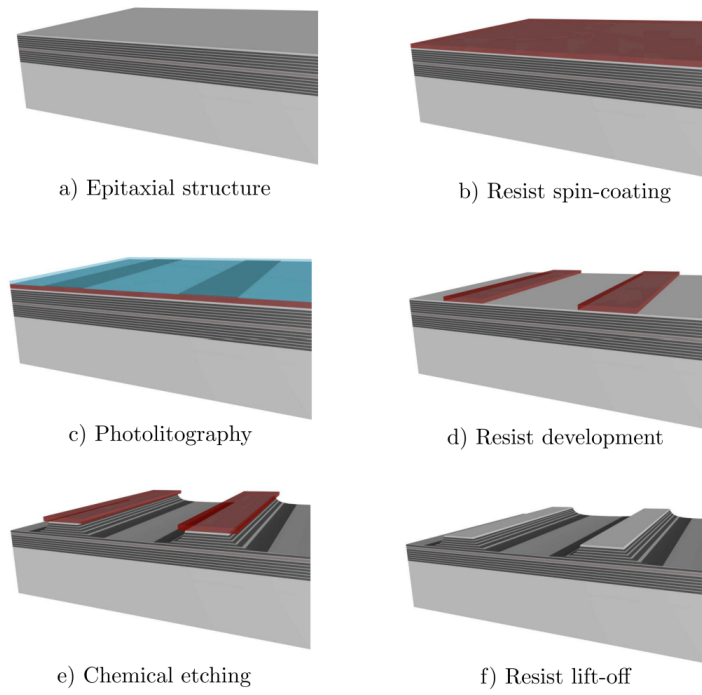


Figure 22: Schematic representation of the fabrication process. Reproduced from [22]

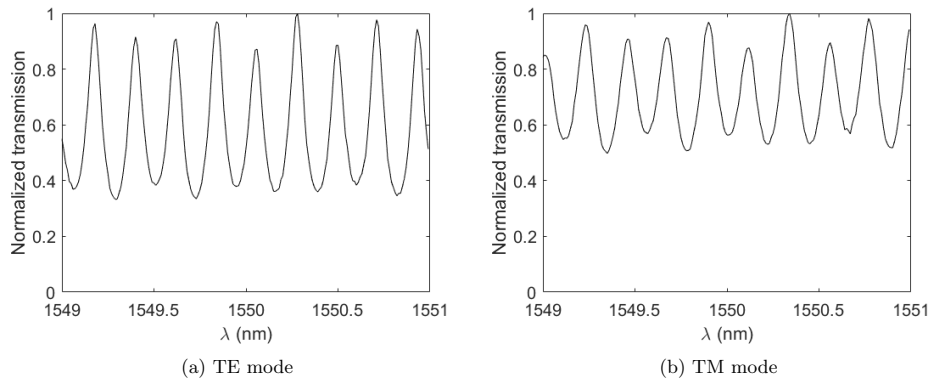


Figure 23: Fabry-Pérot transmission spectra of guide 20B

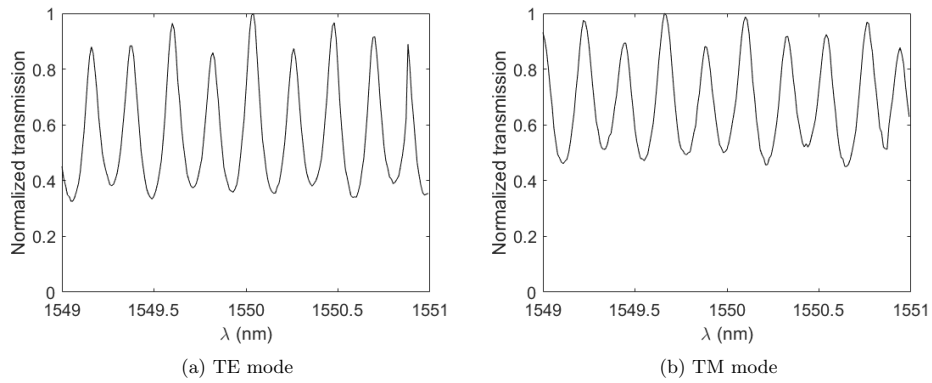


Figure 24: Fabry-Pérot transmission spectra of guide 24M

Guide	TE		TM	
	\tilde{R}	$\alpha(\text{cm}^{-1})$	\tilde{R}	$\alpha(\text{cm}^{-1})$
20B	0.234	1.3228	0.136	3.8016
24M	0.23	1.4197	0.1622	2.0231

Table 7: Results of Fabry-Pérot measurements for the waveguides 20B and 24M

3.3 Measurement of Fabry Pérot spectra after mirror deposition

Sample **K7AD121-L1** was characterized again after the mirror deposition, using the same procedure detailed in Section 3.2. The results for the two best waveguides are listed in Table 8 and Figures 25 and 26 show the experimental Fabry-Pérot spectra.

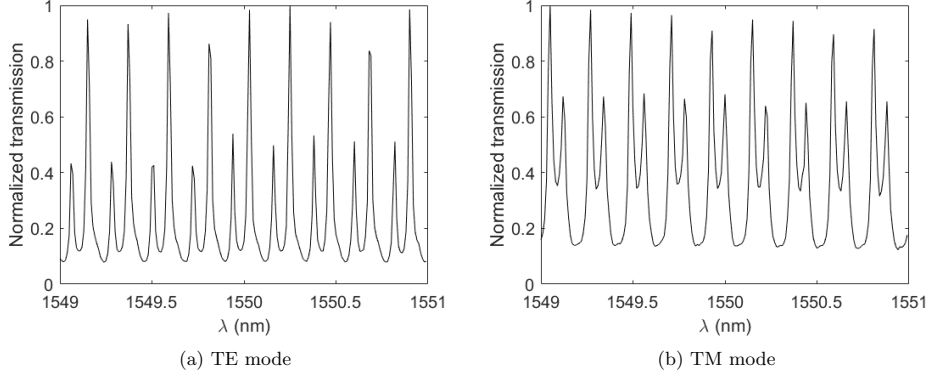


Figure 25: Fabry-Pérot transmission spectra of guide 20B

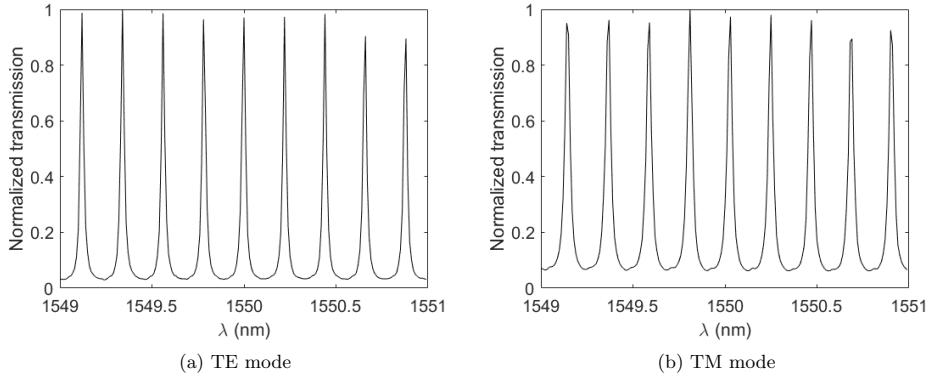


Figure 26: Fabry-Pérot transmission spectra of guide 24M

Guide	TE				TM			
	\tilde{R}	$\alpha(\text{cm}^{-1})$	R	R_{sim}	\tilde{R}	$\alpha(\text{cm}^{-1})$	R	R_{sim}
20B	0.5479	2.9484	0.7138	0.9224	0.4386	3.9154	0.9381	0.875
24M	0.6919	1.6275	0.9191		0.5896	2.3255	0.8837	

Table 8: Fabry-Pérot characterization after mirror deposition

The presence of secondary peaks in the spectra of guide 20B indicates that it is multimodal: we can assume that this feature was already present before the mirror deposition, but the width of the peaks due to the low reflectivity did not allow to resolve them. After the deposition, the peaks became narrow enough to be resolved. The losses of guide 24M are close to the values before the deposition, so it can be used to estimate the lossless mirror reflectivity: assuming that α has the pre-deposition value indicated in Table 7, $R = \tilde{R}e^{\alpha L}$ can be calculated, giving $R_{TE} = 0.9191$ and $R_{TM} = 0.8837$, both very close to the value of my numerical simulations R_{sim} (see Table 4).

4 Photon pairs generation

In this section I describe the experimental setup used for the photon pair generation. The setup had to be remounted, so, in order to verify that it was properly aligned, we mounted sample **F3W083**, which had already been tested. The setup used for photon pair generation is sketched in Figure 27: a Ti:Sa laser emits 4 ps pulses at wavelength $\lambda = 773$ nm; the low power arm of the 99:1 Beam Splitter (BS) is sent to an Optical Spectrum Analyzer (OSA) to check its emission spectrum. The other arm, instead, is sent to the Spatial Light Modulator (SLM) for the beam shaping (as described in [22]) and is then focused on the top of the sample. The setup is equipped with two systems of lenses: the first is a telescope between the laser and the SLM and enlarges the laser spot in order to fully exploit the SLM area, while the second is a 4f setup between the SLM and the sample that reduces back the spot size and allows to report the phase imposed by the SLM on the sample. Finally, the pump beam is focused on the sample by means of a cylindrical lens to match as well as possible the top surface of the waveguide. The photon pairs emitted by the source are collected through microscope objectives, coupled to fibers and sent to the Superconductive Nanowire Single Photon Detector (SNSPD), in turn connected to a Time Tagger (TT); optical longpass filters with a cut-on wavelength of 1400 nm are added to reduce noise.

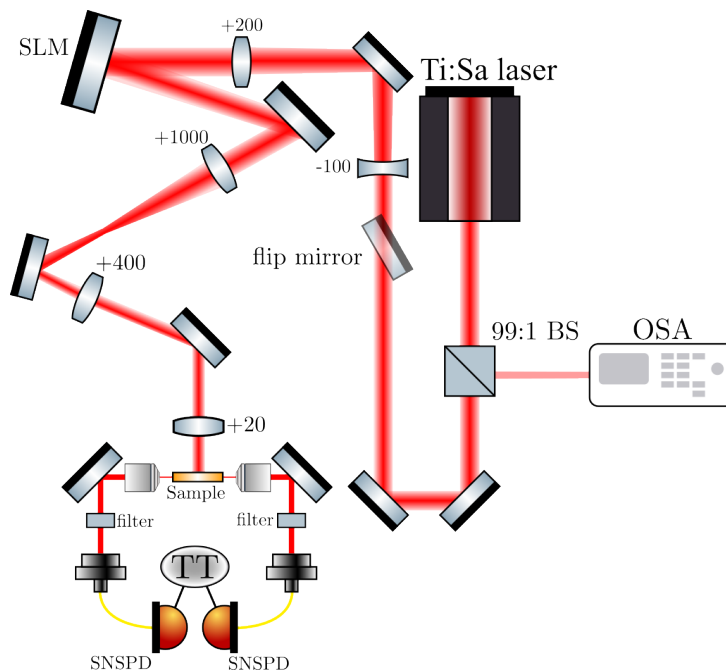


Figure 27: Experimental setup. Lenses' focal lengths are expressed in millimetres

To test that the setup is working properly, we have initially excluded the SLM by means of a flip mirror and mounted an older sample (**F3W083**) to assess the good realignment of the setup, obtaining the coincidence graph in Figure 28. The peak at $\Delta t \simeq 8.5$ ns proves the pair generation, with a Coincidence to Accidental Ratio (CAR) around 48. The fact that the peak is not centred at $\Delta t = 0$ is due to a difference in the optical paths of the setup and can be compensated in data post-processing.

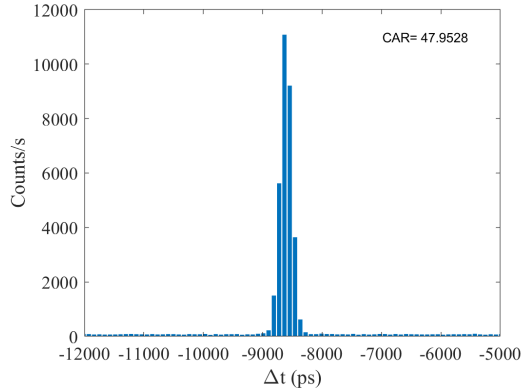


Figure 28: Coincidence histogram obtained with the sample **F3W083**

The next step will be to mount the sample **K7AD121-L1** and characterize its efficiency and the generated quantum state through HOM interference and JSI reconstruction.

5 Conclusions and perspectives

During this internship, I worked on an AlGaAs waveguide source of photon pairs, and in particular on the spectral narrowing of the emitted biphoton state in view of a project of the team focused on the realization of an ion-photon interface. My work involved both numerical simulations and experiments: I started by performing simulations to find the fabrication parameters (i.e. top width and etching depth) that would give good mode confinement inside the waveguide.

In view of the deposition of Bragg mirrors to increase the facet reflectivity, I performed FDTD simulations to calculate the reflectivity as a function of the number of mirrors. Based on these results, I also performed JSI simulations to assess the effect of the mirrors on the emitted biphoton state. This work highlighted that the main sources of distinguishability between the two photons are the difference in modal reflectivity and in effective modal refractive index (birefringence) between the TE and TM modes. To eliminate the birefringence, a waveguide width slightly above $1 \mu\text{m}$ is required, hence a dry etching process must be used, resulting in a waveguide with vertical sidewalls. However, FDTD simulations of this structure show lower reflectivity; further simulations are required to investigate this problem.

Sample **K7AD121-L1** was fabricated by UV lithography and wet etching and I characterized it via the Fabry-Pérot technique, identifying the two best guides in terms of losses. The collaboration with X. Lafosse (C2N) allowed us to identify the materials and number of layers for the Bragg mirrors deposition; for a first trial, three bi-layers $\text{SiO}_2/\text{TiO}_2$ Bragg mirrors were deposited by X. Lafosse by Ion Beam Assisted Deposition (IBAD) at C2N. The characterisation of the sample after the mirror deposition has allowed to deduce reflectivity values $R_{TE} = 0.9191$ and $R_{TM} = 0.8317$, in very good agreement with my numerical simulations.

Subsequently, the setup for the photon pair generation was remounted and tested with an old sample. The coincidence graph proves that the setup works properly. This setup will be used for the experimental measure of sample **K7ADA121-L1**'s JSI via dispersive fiber spectrography [37] [22] to verify the effect of the mirrors on the emitted biphoton state. A HOM experiment will also be done to test the validity of our numerical simulations.

My PhD project will focus on pushing further the spectral narrowing of this source, in view of the realization of an ion-photon interface: this could be achieved by the deposition of more mirrors or by exploiting other degrees of freedom given by this source. We will also work on the implementation of Bell states in different degrees of freedom (for example polarization and frequency), to increase the possibilities of realization of the photon-ion interface. Moreover, pump beam shaping techniques, which were already used to engineer the exchange statistics of the photon pairs, will be further exploited for the realization of highly nonclassical states, such as hyper-entangled polarization-frequency states, cat states and compass states; this work opens promising perspectives in quantum metrology and computing and will be done in collaboration with the theoreticians of the group.

References

- [1] Alain Aspect, Philippe Grangier, and Gérard Roger. “Experimental Tests of Realistic Local Theories via Bell’s Theorem”. In: *Physical Review Letters* 47.7 (Aug. 17, 1981), pp. 460–463. DOI: 10.1103/PhysRevLett.47.460.
- [2] Alain Aspect, Philippe Grangier, and Gérard Roger. “Experimental Realization of Einstein-Podolsky-Rosen-Bohm *Gedankenexperiment* : A New Violation of Bell’s Inequalities”. In: *Physical Review Letters* 49.2 (July 12, 1982), pp. 91–94. DOI: 10.1103/PhysRevLett.49.91.
- [3] J. S. Bell. “On the Einstein Podolsky Rosen Paradox”. In: *Physics Physique Fizika* 1.3 (Nov. 1, 1964), pp. 195–200. DOI: 10.1103/PhysicsPhysiqueFizika.1.195.
- [4] J. Brendel et al. “Pulsed Energy-Time Entangled Twin-Photon Source for Quantum Communication”. In: *Physical Review Letters* 82.12 (Mar. 22, 1999), pp. 2594–2597. DOI: 10.1103/PhysRevLett.82.2594.
- [5] Oliver Benson et al. “Regulated and Entangled Photons from a Single Quantum Dot”. In: *Physical Review Letters* 84.11 (Mar. 13, 2000), pp. 2513–2516. DOI: 10.1103/PhysRevLett.84.2513.
- [6] Laia Ginés et al. “High Extraction Efficiency Source of Photon Pairs Based on a Quantum Dot Embedded in a Broadband Micropillar Cavity”. In: *Physical Review Letters* 129.3 (July 13, 2022), p. 033601. DOI: 10.1103/PhysRevLett.129.033601.
- [7] Jin Liu et al. “A Solid-State Source of Strongly Entangled Photon Pairs with High Brightness and Indistinguishability”. In: *Nature Nanotechnology* 14.6 (6 June 2019), pp. 586–593. DOI: 10.1038/s41565-019-0435-9.
- [8] Daniel Huber et al. “Semiconductor Quantum Dots as an Ideal Source of Polarization-Entangled Photon Pairs on-Demand: A Review”. In: *Journal of Optics* 20.7 (July 1, 2018), p. 073002. DOI: 10.1088/2040-8986/aac4c4.
- [9] Federico Andrea Sabattoli et al. “A Silicon Source of Frequency-Bin Entangled Photons”. In: *Optics Letters* 47.23 (Dec. 1, 2022), pp. 6201–6204. DOI: 10.1364/OL.471241.
- [10] Felicien Appas et al. “Nonlinear Quantum Photonics With AlGaAs Bragg-Reflection Waveguides”. In: *Journal of Lightwave Technology* 40.23 (Dec. 1, 2022), pp. 7658–7667. DOI: 10.1109/JLT.2022.3214466.
- [11] Félicien Appas et al. “Broadband Biphoton Generation and Polarization Splitting in a Monolithic AlGaAs Chip”. In: *ACS Photonics* (Mar. 31, 2023), acsphotonics.2c01900. DOI: 10.1021/acsphotonics.2c01900. arXiv: 2208.14108 [quant-ph].
- [12] Robert W. Boyd. *Nonlinear Optics Ed. 3*. Elsevier Science, 2008.
- [13] A. Ashkin, G. D. Boyd, and D. A. Kleinman. “PHASE-MATCHED SECOND-HARMONIC GENERATION IN KDP WITHOUT DOUBLE REFRACTION”. In: *Applied Physics Letters* 6.9 (May 1965), pp. 179–180. DOI: 10.1063/1.1754223.
- [14] M Houe and P D Townsend. “An Introduction to Methods of Periodic Poling for Second-Harmonic Generation”. In: *Journal of Physics D: Applied Physics* 28.9 (Sept. 14, 1995), pp. 1747–1763. DOI: 10.1088/0022-3727/28/9/001.
- [15] Fabien Boitier et al. “Electrically Injected Photon-Pair Source at Room Temperature”. In: *Physical Review Letters* 112.18 (May 7, 2014), p. 183901. DOI: 10.1103/PhysRevLett.112.183901.
- [16] Jianwei Wang et al. “Gallium Arsenide (GaAs) Quantum Photonic Waveguide Circuits”. In: *Optics Communications* 327 (Sept. 2014), pp. 49–55. DOI: 10.1016/j.optcom.2014.02.040.
- [17] Mario Schwartz et al. “Fully On-Chip Single-Photon Hanbury-Brown and Twiss Experiment on a Monolithic Semiconductor–Superconductor Platform”. In: *Nano Letters* 18.11 (Nov. 14, 2018), pp. 6892–6897. DOI: 10.1021/acs.nanolett.8b02794.
- [18] S. Gehrsitz et al. “The Refractive Index of Al_xGa_{1-x}As below the Band Gap: Accurate Determination and Empirical Modeling”. In: *Journal of Applied Physics* 87.11 (June 1, 2000), pp. 7825–7837. DOI: 10.1063/1.373462.
- [19] M. Ohashi et al. “Determination of Quadratic Nonlinear Optical Coefficient of Al_xGa_{1-x}As System by the Method of Reflected Second Harmonics”. In: *Journal of Applied Physics* 74.1 (July 1, 1993), pp. 596–601. DOI: 10.1063/1.355272.

- [20] S. J. B. Yoo et al. “Quasi-phase-matched Second-harmonic Generation in AlGaAs Waveguides with Periodic Domain Inversion Achieved by Wafer-bonding”. In: *Applied Physics Letters* 66.25 (June 19, 1995), pp. 3410–3412. DOI: 10.1063/1.113370.
- [21] X. Yu et al. “Efficient Continuous Wave Second Harmonic Generation Pumped at 1.55 μm in Quasi-Phase-Matched AlGaAs Waveguides”. In: *Optics Express* 13.26 (Dec. 26, 2005), pp. 10742–10748. DOI: 10.1364/OPEX.13.010742.
- [22] Saverio Francesconi. “On-Chip Generation of High-Dimensional Entangled States of Light”. PhD thesis. Université Paris Cité, Dec. 14, 2020.
- [23] Xavier Caillet. “Une Microcavité Semiconductrice Source de Photons Jumeaux Contrapropageants à Température Ambiante”. PhD thesis. Université Paris Diderot, 2009.
- [24] Yeh Albert Pochi. *Optical Waves in Layered Media*. Wiley Series in Pure and Applied Optics. Hoboken (New Jersey): John Wiley & Sons, 2005.
- [25] Born Max. *Principles of Optics: Electromagnetic Theory of Propagation, Interference and Diffraction of Light*. In collab. with Wolf Emil. Seventh (expanded) edition. Cambridge New York Oakleigh: Cambridge University Press, 1999.
- [26] S. Francesconi et al. “Engineering Two-Photon Wavefunction and Exchange Statistics in a Semiconductor Chip”. In: *Optica* 7.4 (Apr. 20, 2020), p. 316. DOI: 10.1364/OPTICA.379477.
- [27] Saverio Francesconi et al. “Anyonic Two-Photon Statistics with a Semiconductor Chip”. In: *ACS Photonics* 8.9 (Sept. 15, 2021), pp. 2764–2769. DOI: 10.1021/acsp Photonics.1c00901.
- [28] Yasser Jeronimo-Moreno, Saul Rodriguez-Benavides, and Alfred B. U’Ren. “Theory of Cavity-Enhanced Spontaneous Parametric Downconversion”. In: *Laser Physics* 20.5 (May 2010), pp. 1221–1233. DOI: 10.1134/S1054660X10090409. arXiv: 1006.0050 [quant-ph].
- [29] Guillaume Boucher. “Biphoton Frequency-Correlations Engineering and Measurement with a Semiconductor Microcavity”. PhD thesis. Université Paris Diderot, 2016.
- [30] C. K. Hong, Z. Y. Ou, and L. Mandel. “Measurement of Subpicosecond Time Intervals between Two Photons by Interference”. In: *Physical Review Letters* 59.18 (Nov. 2, 1987), pp. 2044–2046. DOI: 10.1103/PhysRevLett.59.2044.
- [31] Frédéric Bouchard et al. “Two-Photon Interference: The Hong–Ou–Mandel Effect”. In: *Reports on Progress in Physics* 84.1 (Jan. 1, 2021), p. 012402. DOI: 10.1088/1361-6633/abcd7a.
- [32] P. J. Martin. “Ion-Assisted Thin Film Deposition and Applications”. In: *Vacuum*. Special Issue Vacuum, Electron and Ion Technologies Papers from the Fourth Bulgarian Summer School, Sozopol, Bulgaria, 7-11 October 1985 36.10 (Oct. 1, 1986), pp. 585–590. DOI: 10.1016/0042-207X(86)90325-8.
- [33] James K. Hirvonen. “Ion Beam Assisted Thin Film Deposition:” in: *Materials and Processes for Surface and Interface Engineering*. Ed. by Yves Pauleau. NATO ASI Series. Dordrecht: Springer Netherlands, 1995, pp. 307–346. DOI: 10.1007/978-94-011-0077-9_9.
- [34] Özlem Duyar, Frank Placido, and H Zafer Durusoy. “Optimization of TiO_2 Films Prepared by Reactive Electron Beam Evaporation of Ti_3O_5 ”. In: *Journal of Physics D: Applied Physics* 41.9 (May 7, 2008), p. 095307. DOI: 10.1088/0022-3727/41/9/095307.
- [35] Duo Shu Wang et al. “Research on Influence of Ion-Assisted Deposition to the Optical and Mechanical Properties of SiO_2 Film”. In: *Materials Science Forum* 654–656 (June 2010), pp. 1720–1723. DOI: 10.4028/www.scientific.net/MSF.654-656.1720.
- [36] Alfredo De Rossi et al. “Measuring Propagation Loss in a Multimode Semiconductor Waveguide”. In: *Journal of Applied Physics* 97.7 (Apr. 2005), p. 073105. DOI: 10.1063/1.1873059.
- [37] Malte Avenhaus et al. “Fiber-Assisted Single-Photon Spectrograph”. In: *Optics Letters* 34.18 (Sept. 15, 2009), pp. 2873–2875. DOI: 10.1364/OL.34.002873.